




# Combination of Time Series of L-, C-, and X-Band SAR Images for Land Cover and Crop Classification

Mario Busquier , Graduate Student Member, IEEE, Juan M. Lopez-Sanchez , Senior Member, IEEE, Francesca Ticconi, and Nicolas Floury 

**Abstract**—The availability of new Earth observation satellites operating radar sensors at different frequencies enables the combination of multiple dimensions of the data (time, frequency, polarimetry, and interferometry) in many applications. Image classification is expected to benefit from the diversity of observation. This work illustrates classification experiments carried out with series of images acquired by ALOS-2 PALSAR (L-band), Sentinel-1 (C-band), and TanDEM-X (X-band) in two application domains: 1) land cover classification and 2) crop-type mapping. Their usage, both separately and in combination, serves to identify the complementarity of information. In this work, we propose a new color representation of the pairwise class separability in the case of using three frequency bands, which help identify which bands (or combinations of them) provide the best performance. Results in terms of accuracy scores (overall and class-specific) show that the use of the three frequency bands always outperforms the individual bands and their pairs. In addition, for both land classification and crop-type mapping the accuracy of using coherence time series is lower than the one obtained with the intensity time series, but there is complementarity in terms of sensitivity when both coherence and intensity time series are used together. The classes which are most benefited at each particular case of study have been identified. Finally, a partial tradeoff has been found between the use of multiple frequency bands and the length of the available time series.

**Index Terms**—Crop classification, interferometry, land cover classification, synthetic aperture radar (SAR), time series.

## I. INTRODUCTION

**S**YNTHETIC aperture radar (SAR) satellite sensors are known to provide data with diverse dimensions which can be exploited in many Earth observation applications. The most obvious dimension is radiometry, i.e., the intensity of the image, which depends obviously on the properties of the elements present in the scene. This is usually complemented by polarimetry, i.e., by taking into account the changes in the

wave polarization produced by the scene [1], [2], which is very useful for solving ambiguities present in the intensity images. Polarimetric observables are sensitive to physical properties of the observed targets (i.e., shape, orientation, and dielectric characteristics) and to the scattering properties (e.g., whether there are odd or even bounces, presence of volume scattering, etc.). For this purpose, dual-, compact-, or quad-pol systems are used [3]. An additional dimension with sensitivity to the scene properties is interferometry. SAR interferometry [4], [5] provides information about the vertical distribution of elements in the scene and also serves as an effective change detection technique. Finally, SAR satellites offer also consistent and reliable observation schedules thanks to their nearly all-weather operation and sun-light independence. As a result, long time series of images can be constructed, which contribute to refresh information with short gaps (e.g., six days in case of Sentinel-1) which is a key aspect in many operational applications, such as crop monitoring [6].

Besides polarimetry, interferometry, and time series, there exists an extra data dimension which can be exploited but has received a limited attention in the past: multifrequency. L-, C-, and X-band space-borne SAR systems, such as Sentinel-1, Advanced Land Observing Satellite/Phased-Array L-Band SAR (ALOS/PALSAR), ALOS-2/PALSAR-2, TerraSAR-X, TanDEM-X (TerraSAR-X add-on for digital elevation measurement), COSMO-SkyMed (CONstellation of small Satellites for the Mediterranean basin Observation), SAOCOM (Satélite Argentino de Observación Con Microondas), Radarsat-2, and others are currently in operation, and new ones are planned in the near future, e.g., ROSE-L (Radar Observation System for Europe in L-band), PALSAR-3, NISAR (NASA-ISRO SAR), BIOMASS, etc. This will allow to observe a scene at different wavelengths, different acquisition geometries, and different times. The microwave interaction with the observed scene changes according to frequency mainly due to the fact that the contribution to the radar signal comes from those vegetation elements whose dimensions are of the same order of magnitude of the wavelength. Furthermore, the penetration depth varies as well. Therefore, the multifrequency dimension of radar data shows a clear potential in many applications. In this context, this work is aimed at analyzing the contribution of multifrequency SAR data, including also time series and interferometry, to classification. For this purpose, two application scenarios are studied: 1) general land cover classification and 2) agricultural crop classification.

Manuscript received 5 May 2022; revised 12 July 2022 and 18 August 2022; accepted 9 September 2022. Date of publication 19 September 2022; date of current version 30 September 2022. This work was supported in part by the European Space Agency under Contract 4000133590/20/NL/AS/hh, and in part by the Spanish Ministry of Science and Innovation (State Agency of Research, AEI) and the European Funds for Regional Development under Project PID2020-117303GB-C22. (Corresponding author: Juan M. Lopez-Sanchez.)

Mario Busquier and Juan M. Lopez-Sanchez are with the Institute for Computer Research (IUII), University of Alicante, 03080 Alicante, Spain (e-mail: mario.busquier@ua.es; juanma-lopez@ieee.org).

Francesca Ticconi and Nicolas Floury are with the European Space Agency, ESA-ESTEC, 2201 AZ Noordwijk, The Netherlands (e-mail: Francesca.Ticconi@esa.int; nicolas.floury@esa.int).

Digital Object Identifier 10.1109/JSTARS.2022.3207574

In the rest of this Introduction, the existing examples of combination of polarimetry, interferometry, multifrequency, and time series for land cover classification and crop-type mapping are reviewed. First, it is important to state that the joint exploitation of the four axes of data diversity has not been addressed in the literature. However, it is common to combine two of these axes, and in some cases up to three of them, in classification studies.

In general land cover classification, although there are some examples of comparison of the classification performance of different polarimetric modes at different frequency bands [7], there are only a few in which the different bands are effectively combined to enhance the classification result. The combination of L-, C-, and X-band was successfully tested in [8] for general land cover classification using a single image at each band acquired by ALOS-PALSAR, Radarsat-2, and TerraSAR-X. The joint use of the images acquired at all three bands and exploiting polarimetric observables demonstrated to achieve an overall accuracy (OA) of 98% in an area with eight different land covers. Using only L- and C-band the OA was 96%, whereas individual bands provided OA values not higher than 90%. In that study, the three images were not acquired simultaneously, but with gaps of one and three years among them. Consequently, it was assumed that the land covers were stable in time, which on many occasions is not fulfilled. In any case, the complementary contribution of different frequency bands to land cover classification was already demonstrated in that experiment but deserves further exploration. Multitemporal datasets of the same three bands were evaluated for tropical land cover classification in [9], concluding that multifrequency classification is preferred over multitemporal composites obtained with a single frequency.

Regarding crop-type mapping, also L-, C-, and X-band were used in [10], whereas P-, L-, and C-band were combined in [11] and [12], and L- and C-band were combined in [13] and [14]. In all cases, the classification performance improved when multiple bands were employed with respect to single bands, thanks to the commented complementarity of sensitivity as a function of the wavelength. The sensitivity of the frequency bands to the specific properties of different crops and their evolution along the growing season has been studied by means of airborne SAR campaigns. In [15], the scattering mechanisms present at L-, C-, and X-band in the polarimetric response of corn and barley at different phenological stages were identified, and their change as a function of crop development was assessed. For instance, some changes like the fruit maturation in barley are almost invisible at L-band, while they are observed as strong changes in C- and X-band. These changes are produced mainly in elements of small size (development of spikes) and hence do not really affect L-band waves with a wavelength of 23 cm. On the other hand, changes due to harvest appear as a decrease in backscattering at L- and C-band (due to the reduced volume scattering), whereas they produce an increased echo at X-band caused by an increase in surface scattering.

The exploitation of time series of radar data for crop classification is also well documented in the literature [13], [14], [16], [17], [18], [19]. Notably, the combination of time series of polarimetric observables acquired at L- and C-band was evaluated for crop-type mapping in [13], [14], [16], while C-

and X-band data were combined in [18] and [19]. The main conclusion of these studies was that the most relevant axis for this specific application is time, since crops exhibit specific cultivation calendars and, therefore, their radar responses change with time and differently for each crop species. Therefore, there are sets of dates which serve to separate sets of crops, and this situation changes along time and among crops. In fact, when the observation period covered by the time series includes images acquired before sowing and after harvest, results are usually better than when they are all comprised within the growth season. In addition, the inclusion of the two frequency bands was also beneficial for the classification performance.

SAR interferometric products derived from ERS-1 and ERS-2 data were first employed for land cover classification in [20] and [21]. These pioneering works showed clearly that there was more information content in the time series of interferometric coherence than in the backscatter intensity. Much more recently, thanks to the availability of long time series of Sentinel-1 images, more complete results have been obtained in [22] and [23], which demonstrate the contribution of repeat-pass interferometric coherence for land cover mapping, its complementarity with respect to backscatter intensity, and, moreover, the independence of this contribution with respect to the classifier. In addition, the two available polarimetric channels (VV and VH) provide different information, also complementing the potential of this information source for classification. In the same vein, the usefulness of the time series of six-day Sentinel-1 interferometric coherence for crop-type mapping has been demonstrated in [24].

From this review, one concludes that there are some options which have not been tested yet, mainly those comprising the use of multiple frequency bands, since they have not been combined with interferometry for any classification application, and only in a limited way with time series. In addition, time series of backscatter (intensity) data acquired at several frequency bands have been evaluated for general land cover classification only in a few works, despite the excellent performance found for crop-type mapping. This work is aimed to investigate and assess the complementarity and synergy of multispectral SAR data, from L-, C-, and X-band, including time series and interferometry, for both land cover and crop classification. In summary, the main motivation of this work is the exploration of the added value of multifrequency radar data for classification, which is a subject that has attracted little attention in the past but shows a huge potential in the next future thanks to the increasing number of SAR missions. The study carried out in this work comprises two test sites dedicated to general land cover classification (8 classes) and crop mapping (16 crop types and fallow), respectively. All available images of a single year (2017) from three different satellites are considered.

It must be pointed out that the exploitation of polarimetry, i.e., using diverse polarimetric features as inputs for the classifier, has not been considered in this study because, as it will be shown in Section II, the radar data available at the three frequency bands correspond to three different combinations of dual-pol channels: HH-HV at L-band, VV-VH at C-band, and HH-VV at X-band. As a result, the lack of coincidence in the channels prevents a fair comparison of the contribution of polarimetry at



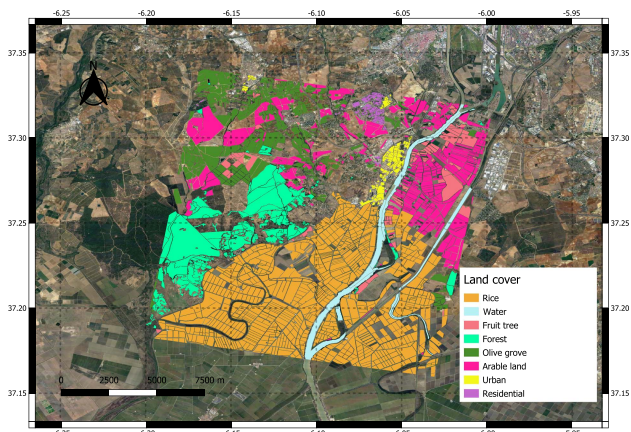


Fig. 1. Land cover map with all polygons selected in the reference data.

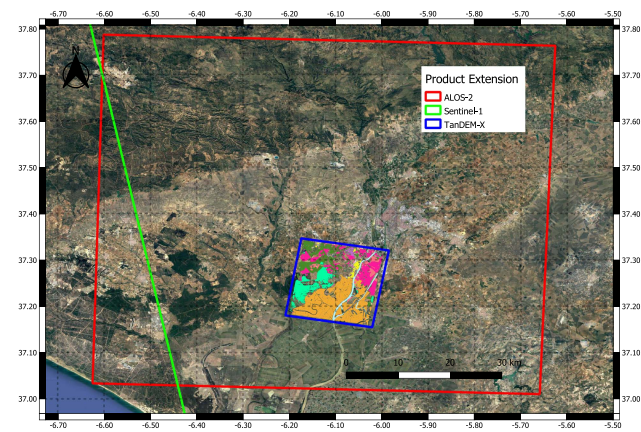


Fig. 2. Coverage of the images provided by the three sensors (ALOS-2, Sentinel-1, and TanDEM-X) on the land cover test site.

TABLE I  
NUMBER OF POLYGONS AND TOTAL AREA PER LAND COVER TYPE IN THE TEST SITE

Land cover type	Total number of polygons	Area (ha)
Rice	903	5919.35
Water	24	662.38
Fruit tree	97	606.93
Forest	166	2137.45
Olive grove	378	1862.36
Arable land	392	2532.11
Residential	61	102.27
Urban area	80	185.38

the three bands. Therefore, since the focus of this study is on the multifrequency aspect, the analysis is limited to time series of backscattering coefficient and repeat-pass interferometric coherence at individual channels.

## II. MATERIALS AND METHODS

### A. Test Sites

Two different geographical locations have been used as test sites for classification purposes. The first test site includes land cover classes, such as urban, forest, water streams, etc. so it is well suited for general classification, whereas the second test site is only devoted to agricultural crops.

1) *Land Cover*: The land cover test site is an area of  $15 \times 15$  km in the Seville province (SE Spain), centred at coordinates 37.25 N, 6.1 W. The layout of all classes present in this site is shown in Fig. 1. The reference data are taken from the official cadastral database. The dataset available for 2017 comprises a total of eight classes which include urban and residential areas, forest, olive groves, fruit tree plantations, arable land, rice fields, and water bodies. The water class refers mainly to the Guadalquivir river, and associated channels, which cross the region from North to South. The class labels are assumed to be valid for the whole observation period, i.e., the entire 2017. All the land cover classes are stable, and they may change only in a small portion along the year (e.g., by a new building in the urban area).

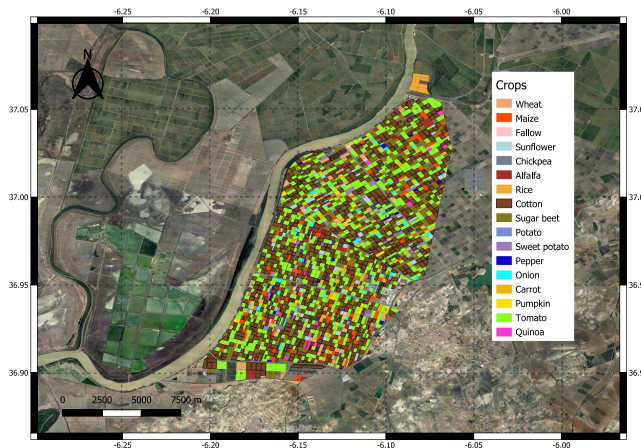


Fig. 3. Crop-type map with all fields selected in the reference data.

Table I presents the number of polygons and total surface corresponding to each class. In this region the data are not balanced, since one class (rice) covers almost half the extension of the zone. This is in contrast to other classes, such as water and fruit trees which only feature 24 and 97 polygons, respectively, and hence a much smaller associated area.

This test site was selected by taking into account the overlapped coverage of the three available sensors (ALOS-2, Sentinel-1, and TanDEM-X). Their coverage and the reference data are shown in Fig. 2. The coverage of Sentinel-1 and ALOS-2 is very wide, but the available TanDEM-X products limit the selected common area.

2) *Crop-Type Mapping*: For crop-type mapping, the test site is part of an agricultural area located also in Seville, Spain, which is labeled as *BXII sector* by the regional administration. This site is south of the land-cover one, and the reference data are also from 2017. All the crops available in the reference data and their distribution over the region are shown in Fig. 3. The reference dataset is extracted from the official land parcel identification system (SIGPAC in Spanish). The area features a very wide range of crop categories, from the total of which 17 classes (16 crop types and fallow) are selected. The crop calendar is shown

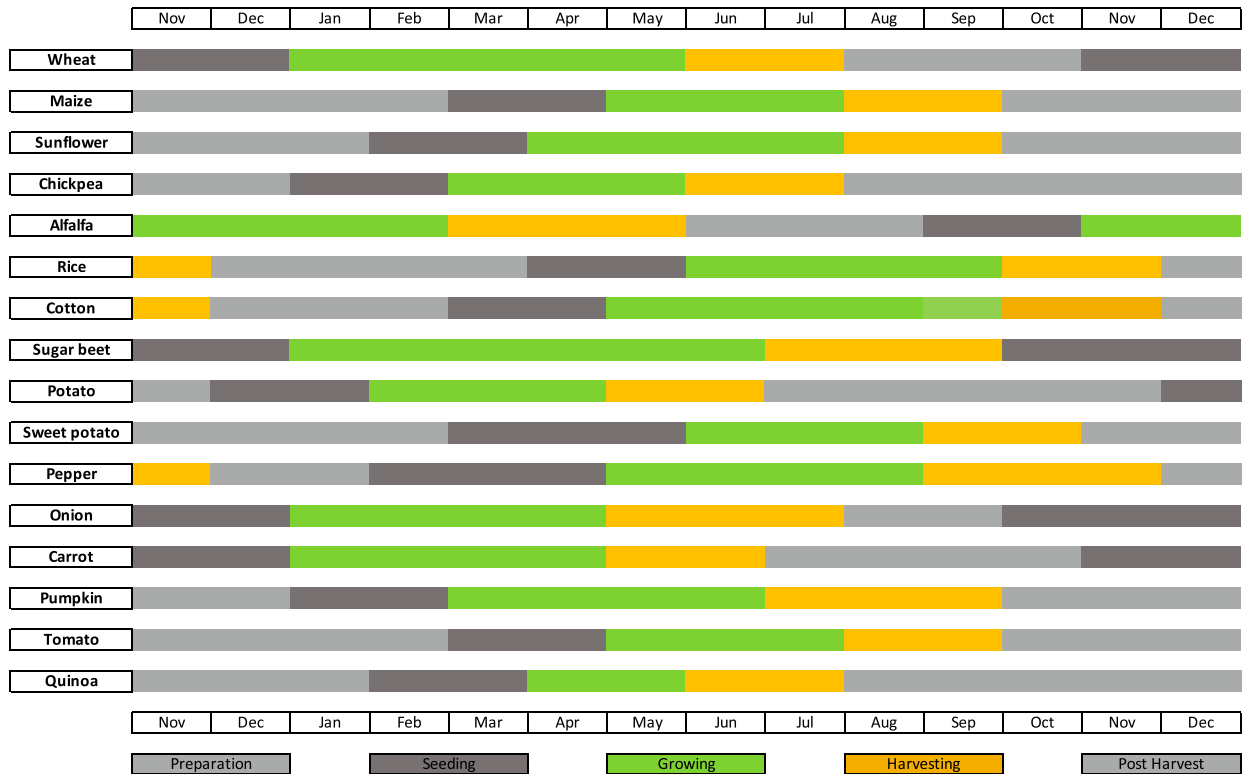


Fig. 4. Crop calendar for the 16 crop types studied in 2017.

TABLE II  
NUMBER OF FIELDS AND TOTAL AREA PER CROP TYPE IN THE TEST SITE

Crop type	Total number of fields	Area (ha)
Wheat	77	284.13
Maize	117	399.62
Fallow	98	80.33
Sunflower	74	220.69
Alfalfa	37	166.50
Rice	9	78.14
Cotton	945	4021.03
Sugar beet	403	1380.35
Potato	20	42.57
Sweet potato	38	110.94
Pepper	31	60.92
Onion	49	121.82
Carrot	72	214.96
Pumpkin	26	93.04
Tomato	659	2616.79
Quinoa	29	72.14

in Fig. 4. There are winter crops, such as sugar beet, wheat, and quinoa, and spring crops like corn, rice and tomato. Except for alfalfa, which is characterized as a multiannual crop, the remaining ones are cultivated only once a year. As a result, and attending to their crop calendar, the labels of the crop classes assigned to every field are assumed to be valid over the whole observation period.

The number of fields and total area of each crop type are shown in Table II. Reference data for 2017 is very heterogeneous regarding the number of fields per crop. The major classes are cotton, tomato, and sugar beet. This unbalance, which is present

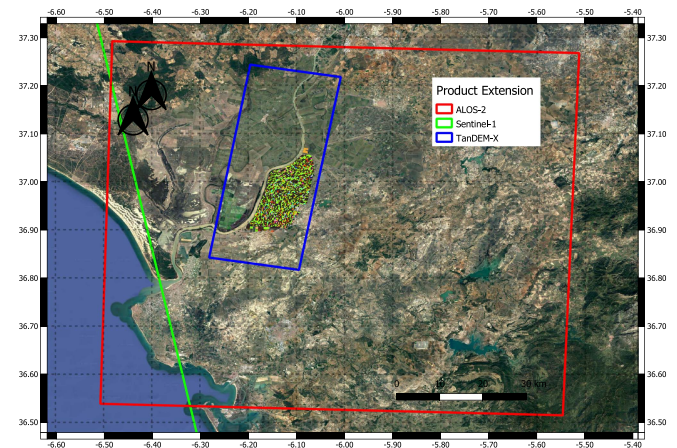


Fig. 5. Coverage of the images provided by the three sensors (ALOS-2, Sentinel-1, and TanDEM-X) on the crop test site.

also in the land cover case, is relevant and will be taken into account in the classification process.

Fig. 5 shows the coverages of the three sensors over the region of interest. While ALOS-2 and Sentinel-1 cover completely the BXII sector and have a very wide coverage, the TanDEM-X images limit the study site because they do not cover the whole BXII sector. Consequently, the area overlapped by the three sensors does not cover the whole crop region, and the reference data were cut to fit the imaged scene.

		2017																														
January	1	2	3	4	5	6	7	8	9	10	11	12	13	14	15	16	17	18	19	20	21	22	23	24	25	26	27	28	29	30	31	
February	1	2	3	4	5	6	7	8	9	10	11	12	13	14	15	16	17	18	19	20	21	22	23	24	25	26	27	28	29	30	31	
March	1	2	3	4	5	6	7	8	9	10	11	12	13	14	15	16	17	18	19	20	21	22	23	24	25	26	27	28	29	30	31	
April	1	2	3	4	5	6	7	8	9	10	11	12	13	14	15	16	17	18	19	20	21	22	23	24	25	26	27	28	29	30	31	
May	1	2	3	4	5	6	7	8	9	10	11	12	13	14	15	16	17	18	19	20	21	22	23	24	25	26	27	28	29	30	31	
June	1	2	3	4	5	6	7	8	9	10	11	12	13	14	15	16	17	18	19	20	21	22	23	24	25	26	27	28	29	30	31	
July	1	2	3	4	5	6	7	8	9	10	11	12	13	14	15	16	17	18	19	20	21	22	23	24	25	26	27	28	29	30	31	
August	1	2	3	4	5	6	7	8	9	10	11	12	13	14	15	16	17	18	19	20	21	22	23	24	25	26	27	28	29	30	31	
September	1	2	3	4	5	6	7	8	9	10	11	12	13	14	15	16	17	18	19	20	21	22	23	24	25	26	27	28	29	30	31	
October	1	2	3	4	5	6	7	8	9	10	11	12	13	14	15	16	17	18	19	20	21	22	23	24	25	26	27	28	29	30	31	
November	1	2	3	4	5	6	7	8	9	10	11	12	13	14	15	16	17	18	19	20	21	22	23	24	25	26	27	28	29	30	31	
December	1	2	3	4	5	6	7	8	9	10	11	12	13	14	15	16	17	18	19	20	21	22	23	24	25	26	27	28	29	30	31	

■ ALOS-2  
■ Sentinel-1  
■ TanDEM-X

Fig. 6. Calendar of acquisitions for the three bands during 2017.

### B. Radar Datasets and Preprocessing

As it has been advanced in the previous subsection, all radar images were acquired in 2017. The exact dates of acquisition of all available images from the three sensors are shown in Fig. 6. The properties of the images of each sensor and the processing carried out are detailed in the rest of this section.

1) *ALOS-2 Data*: L-band data are provided by ALOS-2. As shown in Fig. 6, the acquisition schedule of this satellite provides seven images available over the study region for the whole of 2017. They are mainly concentrated in spring and summer (May to September), with only one extra image in February.

ALOS-2 is a Japanese satellite which features an L-band SAR system (PALSAR-2) operating at a centre frequency of 1.2 GHz. It has full-pol capabilities, implying that it is possible to image the Earth with all linear polarization channels (HH, HV, VV, and VH). In our dataset, all products are dual-pol (HH + HV) with the exception of the one full-pol image acquired on May 3, 2017. The dual-pol images were acquired by using the fine beam double polarization (FBD) mode, characterized for featuring a pixel size of  $3.4 \times 4.3$  m (azimuth  $\times$  slant-range). The spatial resolution is about  $5.3 \times 9.1$  m (azimuth  $\times$  slant-range). The only full-pol image was acquired in the high-sensitive beam quadrature polarimetry (HBQ) mode whose pixel size is  $2.8 \times 2.9$  m (azimuth  $\times$  slant-range). The corresponding spatial resolution is about  $4.3 \times 5.1$  m (azimuth  $\times$  slant-range). In order to create a consistent and common dataset, all images were constrained to the HH and HV channels during the preprocessing.

The preprocessing of the L-band dataset was carried out using the SNAP software provided by the European Space Agency (ESA) and consists of the following steps: 1) calibration, 2) subset of the region of interest, 3) speckle filtering using a  $9 \times 5$  boxcar filter (azimuth  $\times$  slant-range), 4) linear-to-dB transformation, and 5) geocoding by using a UTM grid with 5-m pixel spacing. The selection of the window size for the boxcar filter is based on providing enough speckle filtering and not compromising the resulting spatial resolution. The resulting equivalent number of looks is around 14 for the FBD images and 16 for the HBQ image. The number of pixels employed by the filter is similar for all sensors (from 45 to 49). The shape in each case, e.g.,  $9 \times 5$  for ALOS-2, is decided according to the pixel size of each sensor and with the objective of producing pixels of approximately square shape at the output, since they are used later for geocoding on a regular grid.

As the polarimetric channels available in the three frequency bands are different, as detailed later for C- and X-band, the polarimetric information was restricted to the intensity (backscattering coefficient,  $\sigma_0$ ) of the two available channels, i.e., HH and HV in the L-band case, which will be later used as input features for classification.

It should be clarified that a coregistration step was not necessary in the preprocessing of ALOS-2 data to combine different acquisitions from dates, relying on the geocoding for that purpose. Geocoding was carried out with data resulting from the boxcar speckle filter, i.e., with an effective pixel size (pixel spacing  $\times$  kernel size) of around 30 m in both dimensions. The precision provided by geocoding is about 10 m, which is less than the effective pixel size of the speckle-filtered data. Consequently, the geocoding inaccuracy does not affect the performance of the classification undertaken in this study. In addition, for the Sentinel-1 and TanDEM-X datasets the results with and without coregistration were compared, and there was no noticeable difference.

2) *Sentinel-1 Data*: Sentinel-1 is a constellation of two satellites, 1 A and 1B, which are part of the Copernicus program of the European Commission. Thanks to their orbit configuration, this system provides images acquired every six days over Europe. As a result, we have at our disposal a consistent time series formed by 61 images in 2017.

Regarding the sensor, it is an SAR operating at a centre frequency of 5.405 GHz and capable of acquiring dual polarization products (nominally VV and VH over land). Interferometric wide swath (IW) products have been employed. They are acquired in TOPSAR mode (terrain observation with progressive scans SAR), which provides a pixel size of  $13.9 \times 2.3$  m (azimuth  $\times$  slant-range). The corresponding spatial resolution is about  $22 \times 3$  m (azimuth  $\times$  slant-range).

As for the preprocessing, all the images were processed using the SNAP software with the following steps: 1) apply orbit file, 2) calibration, 3) coregistration with respect to a master image (back-geocoding), 4) subset of the region of interest, 5) speckle filtering using a  $3 \times 15$  boxcar filter (azimuth  $\times$  slant-range), 6) linear-to-dB transformation, and 7) geocoding by using a UTM grid with 5-m pixel spacing. The equivalent number of looks obtained is around 22. The resulting products from this preprocessing are the  $\sigma_0$  images for each polarimetric channel (VV and VH) which will be later used as input features in the classification algorithm. In this case we carried out the



coregistration of the images because they were also used for computing interferometric coherence, so in this way the first steps of the processing were common for backscatter and for coherence.

In addition, besides intensity, repeat-pass interferometric coherence will be used later in some experiments. For this purpose, they were also computed, for each polarization channel, by combining images acquired in consecutive passes, i.e., with a six-day temporal baseline. From the set of 61 images, 60 coherences are calculated. The preprocessing steps are as follows: 1) apply orbit file, 2) calibration, 3) coregistration with respect to a master image (back-geocoding), 4) subset of the region of interest, 6) computation of the coherence using a  $3 \times 15$  boxcar filter (azimuth  $\times$  slant-range) with topographic phase removal, and 7) geocoding by using a UTM grid with 5-m pixel spacing. In summary, the C-band dataset comprises 61 intensities and 60 coherences for each channel (VV and VH). It should be noticed that the height of ambiguity provided by the six-day interferograms ranges from 65 to 1130 m. With such large values, the dominating decorrelation source is temporal decorrelation, not volume decorrelation, as will be discussed in Section III.

3) *TanDEM-X Data*: TanDEM-X is the name of TerraSAR-X's twin satellite and also the mission which consists in flying both satellites in a close formation, which makes it possible to image the Earth at the same time with two different incidence angles. The main purpose of this German mission was the generation of a high-precision global digital elevation model (DEM). Typically separated by a baseline from 100 to 300 m, this constellation forms a single-pass SAR interferometer. Working at X-band, the instruments operate at a central frequency of 9.6 GHz, and can image the Earth in both single- and dual-polarization modes. In the standard acquisition mode, one satellite acts as a transmitter and both as a receivers, what allows to obtain both a monostatic and a bistatic image. The revisit time of the system is 11 days, but the acquisitions are commanded on demand and not on a regular monitoring basis (in contrast to Sentinel-1).

From the available dataset in 2017, only the monostatic images were employed, which were acquired in stripmap mode by one of the two satellites, depending on the date. The images were gathered at the two copolar channels, HH and VV. The pixel size is  $2.4 \times 0.9$  m (azimuth  $\times$  slant-range), whereas the spatial resolution is  $6.6 \times 1.1$  m (azimuth  $\times$  slant-range). As for the number of acquisitions, it can be seen in Fig. 6 that this dataset is made up of 20 images taken without any predefined temporal pattern. As in the case of ALOS-2 data, there are several months without imagery, which in this case correspond to January, November, and December.

Although TanDEM-X provides also single-pass interferometric information, with the aim of comparing and combining the same types of data in C- and X-band, we retrieved only the same information as for C-band in the preprocessing: intensity and repeat-pass interferometric coherence. The processing of the X-band images was also carried out with SNAP.

The steps for obtaining the co-polar backscattering coefficients are the following: 1) subset of the region of interest,

2) calibration, 3) coregistration with respect to a master image, 4) speckle filtering using a  $7 \times 7$  boxcar filter, 5) linear-to-dB transformation, and 6) geocoding by using a UTM grid with 5-m pixel spacing. The resulting equivalent number of looks is 15 approximately. As for Sentinel-1, we carried out the coregistration of the images because they were also used for computing interferometric coherence, so in this way the first steps of the processing were common for backscatter and for coherence.

As the temporal sampling of the X-band is not completely regular, we computed the repeat-pass coherence only for those date pairs separated 11 days, i.e., with the minimum available temporal baseline. The coherence preprocessing steps are as follows: 1) subset of the region of interest, 2) calibration, 3) coregistration with respect to a master image, 4) computation of the coherence using a  $7 \times 7$  boxcar filter with topographic phase removal, and 5) geocoding by using a UTM grid with 5-m pixel spacing. From a total of 20 images, only 16 repeat-pass coherence products were obtained. The height of ambiguity provided by the 11-day interferograms ranges from 30 to 310 m. Therefore, as in the Sentinel-1 case, the dominating decorrelation source is temporal decorrelation, not volume decorrelation.

### C. Separability Analysis

The uncertainty associated with all image classification problems comes from the ability of the classification approach to separate or distinguish among the classes under study by exploiting the available set of input data [25]. Before carrying out classification tests, it is convenient to study the class separability by using the available input features. This is especially useful in our study, since we aim at combining features coming from different data sources (radar sensors operating at different frequency bands).

The metric used to conduct this separability analysis is the Jeffries–Matusita (JM) distance [26]. It consists of an estimator, computed for each pair of classes, which indicates their separability given the input data. In the literature, it has been identified as a good indicator of crop separability [27] and used with time series of SAR images [28]. The pairwise JM distance is calculated in the following way:

$$JM_{p,q} = \sqrt{2 \left( 1 - \sum_{i=1}^N \sqrt{p_i \cdot q_i} \right)} \quad (1)$$

where  $p$  and  $q$  are the probability density functions (PDFs) of the data (input features) for two different classes. These PDFs can be computed as the normalized histograms of the radar data for each class, where  $N$  is the number of bins of each histogram. The JM distance obtained using (1) ranges from 0 to  $\sqrt{2}$ . The higher the JM value, the better the separability between a pair of classes.

### D. Classification Strategy

The main goal of our classification experiments is to study the performance and the differences between cases when classifying by using different combinations of features and bands. In that regard, the three frequency bands (L, C, and X) can be used

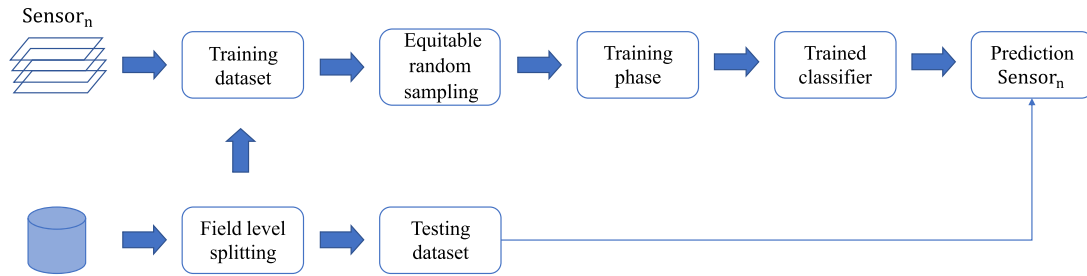


Fig. 7. Algorithm flowchart for the classification with individual frequency bands.

alone, combined in pairs, and all three together. Similarly, when both intensity and coherence are available, they can be used separately or in common.

Most of the examples found in literature, in which multiple SAR data sources are combined, are based on the stacked-vector method [25], i.e., all features coming from the different sources (polarimetric channels, coherences, dates, frequencies, etc.) are used to form the input feature set. This methodology is straightforward and easy to use. However, combining *a posteriori*, i.e., using fusion at decision level, the results of multiple classifiers (one for each independent data source) is also possible (e.g. using Bayesian theory or evidential reasoning [25]) and can produce enhanced results, as recently demonstrated with the fusion of Sentinel-1 and Sentinel-2 data for crop-type mapping [29]. In this work, we have used this approach, so the next two subsections are devoted to describe the classification methodology for individual bands and for the fusion of them, respectively.

1) *Methodology for Individual Frequency Bands*: The flowchart of the classification method used for one band only is depicted in Fig. 7. The classification process is carried out by the random forest (RF) algorithm [30]. It is a state-of-the-art supervised classifier, well known for its good performance. At the same time, it is very widespread in the remote sensing bibliography as it is available on most open-source platforms (e.g. Python and R). Moreover, thanks to the explicit outputs it provides (likelihood vectors), it enables the later use of the product of experts for the fusion of frequency bands (see Section II-D2). Other more advanced algorithms may have advantages in terms of classification and computation time, like the light gradient boosting machine (LGBM). However, for all the mentioned reasons, and since the objective of this work is the evaluation of the input features for classification, and not the classification method itself, RF was selected.

The implementation employed in this work is provided by the scikit-learn package in Python [31] and was run mainly with default parameters. The number of trees was set to 1000 in order to ensure a good performance, but it could have been set to 400–600 to reduce the computation time without modifying the final results [32], [33]. The number of features considered when looking for the best split was left to the default value. The specific strategy for addressing the training data, the prediction, and the evaluation of the accuracy results is explained in the following paragraphs.

In the preprocessing of the radar data there are steps, like speckle filtering and coherence estimation, which entail a degradation of the spatial resolution with respect to the original images. Consequently, the final value at each pixel corresponds to the spatial averaging computed from it and its surrounding neighbors, so pixels which are close together in the same geographical location will be correlated (and will tend to exhibit very similar values). In order to prevent the classifier from having correlated pixels in both training and evaluation sets, we perform an initial split at polygon or field level: 50% of the polygons for each class inside the reference data compose the training dataset and the remaining ones the testing dataset.

After doing the field level splitting there is still a strong imbalance in the number of pixels selected for each class inside the training dataset. As we showed in Section II-A, in both land cover and crop sites, there are classes which have much more fields and surface, hence samples, than others. To balance the training data, we carry out an extra step, called *equitable random sampling* in Fig. 7. It consists in choosing for every class the same number of pixels as the smallest class has. By doing so, all pixels of the smallest class are selected in the training dataset, whereas the pixels of the other classes are selected in the same amount but in a random way. If this were not done, the larger classes would be dramatically benefited in the training phase at the expense of the smaller ones as a result of their overrepresentation inside the training data. In the end, it would lead to unreliable accuracies for each class because of their strong imbalance in terms of number of pixels at the input of the classifier.

Once the training pixels are selected, they are introduced at the input of the classifier starting the training phase in which the decision trees and their logical structure is built. Next up, the trained classifier is applied on the testing data, i.e., the 50% of the polygons for each class resulting from the initial *field level splitting*. As displayed in Fig. 7, the output of the algorithm is the prediction for every pixel of the testing dataset. Specifically, and thanks to the use of the RF algorithm, the output consists in a probability vector, for each testing pixel, indicating its likelihood to pertain to any possible class. Obviously, for the classification with an individual frequency band, the highest probability found in each vector defines the final predicted class chosen for each pixel.

This algorithm is run 10 times, in which a different random field splitting is performed each time. The main purpose is to prevent the final accuracy metrics to be biased, as the accuracies obtained at the end of a single iteration could be the result of a

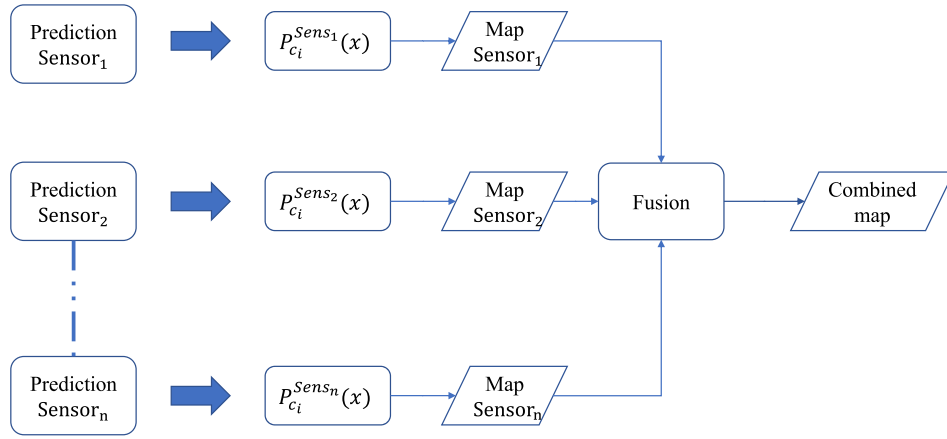


Fig. 8. Algorithm flowchart for the fused classification.

specifically favorable/unfavorable training/test splitting at field level. By running the algorithm ten times, different training and testing datasets are employed, so the final averaged accuracy metrics are reliable.

2) *Fusion Methodology*: The fusion methodology, summarized in Fig. 8, is applied when using two or more frequency bands in the classification. Basically, it consists in a post-processing step performed after having obtained all the probability vectors, for each pixel, from two or more classifiers applied to individual bands.

To begin with, the classifications for the selected bands are performed separately. For this purpose, we first perform the *field level splitting* in the reference data for creating the training and testing datasets. It is important to point out that this splitting is the same for all the classifiers used, as we have to work with the same pixels in all frequency bands.

The equitable random sampling step is then performed following this approach. Again, although pixels are randomly selected on the training data, the random selection applied is the same in all classifiers. As a result, the same pixels are selected in all classifiers. In this way, we work with pixels pointing to the same geographical position in the training and test dataset, but keeping their specific values coming from each band. In addition, with this approach the size of all sets (training and testing) is the same in the fusion methodology and in the classification with individual bands.

Once the classification is finished in the classifier of each individual band, we can compute the fused results by means of the *product of experts* [29]

$$P_{c_i}^{Sens_1, Sens_2, \dots, Sens_N}(x) = \frac{P_{c_i}^{Sens_1}(x) P_{c_i}^{Sens_2}(x) \dots P_{c_i}^{Sens_N}(x)}{\sum_{i=1}^N P_{c_i}^{Sens_1}(x) P_{c_i}^{Sens_2}(x) \dots P_{c_i}^{Sens_N}(x)} \quad (2)$$

where  $P_{c_i}^y(x)$  stands for the likelihood of pixel  $x$  to belong to class  $c_i$  in classifier  $y$ , being  $y$  each one of the sensors  $c$  or available bands (i.e., L-, C-, or X-band). This expression makes use of all the likelihood vectors available for each pixel and let us obtain

a fused vector which will define the final class of each pixel. In this way, we can have three different results with individual bands (L, C, and X), and four possible combinations of bands: 1) L and C, 2) L and X, 3) C and X, and 4) L, C, and X.

3) *Evaluation*: From the prediction results, the evaluation of all combinations of bands and experiments undertaken are based on the confusion matrices computed with all pixels in the testing set. From the confusion matrix, both the overall accuracy (OA) and the F1-score are obtained. OA is the proportion of correctly classified pixels out of the total. The standard deviation of the OA, denoted as  $\sigma$ , has been also computed from the set of ten realizations of the classification and will be shown in the Results section. The F1-score is calculated as the harmonic mean between the producer's accuracy (PA) and the user's accuracy (UA), whose definitions can be found in [34]. Consequently, the F1-score offers information on the accuracy specifically for each class and, therefore, is useful to evaluate how each input dataset contributes to each class in particular.

### III. RESULTS

Before presenting the results obtained, it must be reminded that the usage of data from different SAR sensors in any application of Earth observation is influenced not only by the frequency bands of the sensors, but by other technical aspects which affect the data gathered. Among the other aspects to be considered, it has been already mentioned that the dual-pol combinations available in this study at the three bands do not coincide. This means that when we compare, for instance, L- and C-band, we are using different polarimetric channels (HH versus VV) and they, by definition, already provide different sensitivity. Similarly, the signal-to-noise ratio (SNR), as a measure of the quality of the measured data is very different among sensors. For instance, the noise level of ALOS-2/PALSAR-2 is much lower (i.e., better) than the one of Sentinel-1 and TanDEM-X, so we can expect a better SNR in our L-band data. Using different sensors also entails a varying observation geometry. Consequently, the incidence angle employed in the datasets of the three bands is not the same, and the radar response of any scene is known to



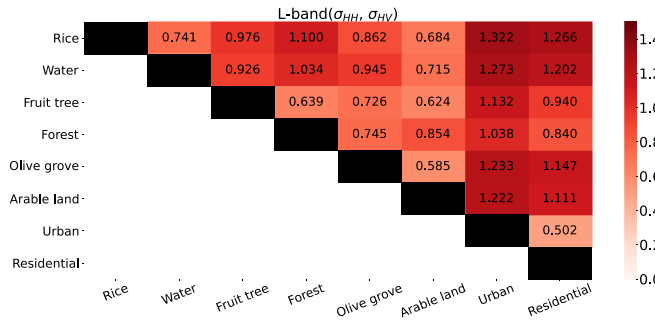


Fig. 9. Separability matrix for land cover at L-band.

be affected by the observation geometry. In summary, despite the results of this section are presented as dependent only on the frequency band for the sake of simplicity, other technical aspects of the sensors and the imaging configuration affect the classification performances obtained and, therefore, should be considered if a more detailed analysis is needed. In this vein, this study really constitutes a *multiplatform* combination instead of a multifrequency one, since frequency band is not the only sensor parameter that changes among the three datasets.

### A. Land Cover

1) *Separability Analysis*: As a preliminary study, we evaluate here the pairwise separability of each frequency band separately. To do so, the JM distances are computed for each possible pair of classes by taking as inputs the intensity time series from each frequency band: HH + HV at L-band, VV + VH at C-band, and HH + VV at X-band. In order to avoid biasing this study by the different lengths of the intensity time series of each frequency band, C- and X-band were decimated to match the time series of L-band. As a result, only seven acquisition dates per band are used. For C- and X-band they correspond to the closest, temporarily speaking, to the ones of L-band.

The pairwise separability values for L-band are shown in Fig. 9. All values range from 0.5 to 1.3. The two classes with best separability with respect to the rest are urban and residential zones, with most JM values above 1. However, the own JM distance between urban and residential is around 0.5, which is a rather low value, but expected at the same time considering that both classes are associated with built-up areas. Rice and water are also well separable from the rest of the classes, whereas the worst separability is found for the rest of vegetation classes: forest, fruit trees, olive grove, and arable land.

The JM values obtained at C-band are shown in Fig. 10, which in general are slightly lower than at L-band. As in the case of L-band, urban zone constitutes the most separable class, followed by residential zones. And, in addition, they show a low separability between them as at L-band. In contrast, water exhibits higher values than at L-band for all classes, and rice shows lower values than at L-band except with respect to water. Regarding the vegetation classes, their relative separability is similar to L-band, but with lower values at C-band.

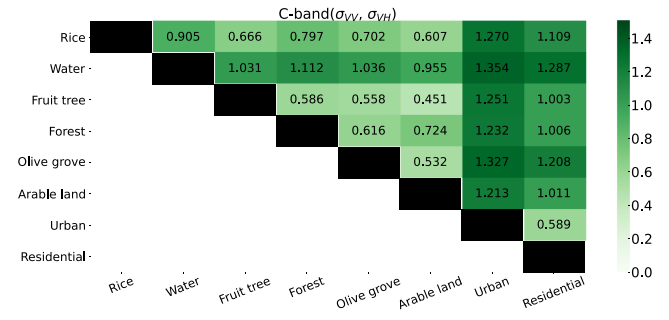


Fig. 10. Separability matrix for land cover at C-band.

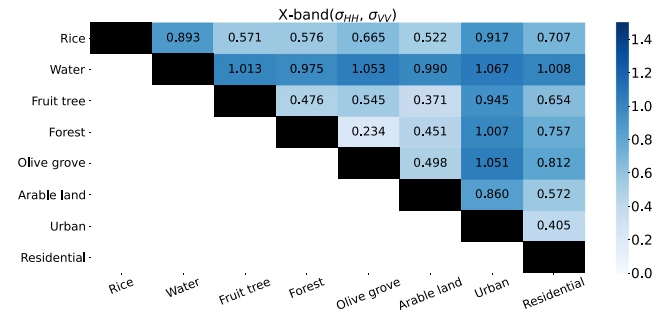


Fig. 11. Separability matrix for land cover at X-band.

Finally, the pairwise separability measured at X-band is depicted in Fig. 11. All values are lower at this band compared to L- and C-band. JM distances for urban and water are the highest ones, followed by residential zones and rice, but they are significantly smaller in this frequency band. The smallest JM value is obtained at X-band for the pair olive grove versus forest in which the separability only reaches 0.234.

As a final analysis the three matrices have been merged into a single figure so as to illustrate jointly their performance and to identify the potential prevalence of some frequency band for distinguishing between classes. This type of representation is an original contribution of this work. The joint figure is an RGB composite of the three separability matrices obtained at L-, C-, and X-band. The JM values of each band are scaled to a grey level (0–255) and then associated with a primary color (red with L-band, green with C-band, and blue with X-band). The resulting color image is the joint representation of the resulting separability matrices, which is shown in Fig. 12. Following this approach, the shade of the resulting color indicates the frequency band or bands that are contributing most to the separability. Primary colors are associated with single bands, secondary colors with combinations of two bands, and grey levels with the three bands.

One can easily appreciate in Fig. 12 that there is a variety of colors, which means that for each class pair the separability provided by the three bands shows a different behavior. Water presents greyish colors with respect to all classes, which means that it is similarly separable at all three bands. Regarding urban and residential areas, the corresponding color with respect to the rest of classes (rightmost two columns) is mostly yellowish,

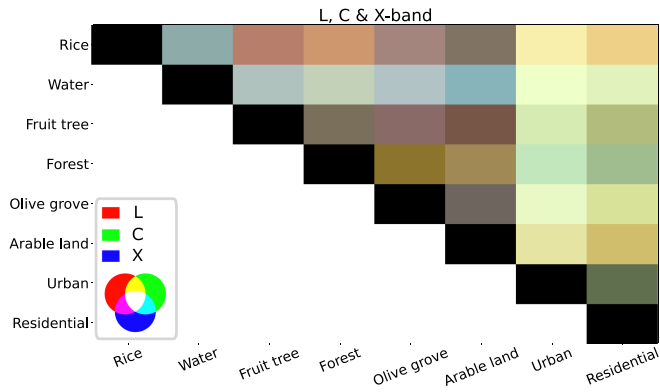


Fig. 12. Joint RGB representation of the three separability matrices obtained for land cover at L-band (red), C-band (green), and X-band (blue).

TABLE III  
OVERALL ACCURACY OBTAINED FOR LAND COVER WITH SEVEN IMAGES PER FREQUENCY BAND

Bands	OA	$\sigma$
L	81.40	1.34
C	78.27	1.37
X	70.79	1.28
L & C	85.11	1.41
L & X	84.95	1.33
C & X	81.59	1.32
L & C & X	86.39	1.30

i.e., L- and C-band (red and green) provide better separability than X-band. As for the vegetation classes (i.e., rice, arable land, forest, fruit trees, and olive grove) their pairwise separability is in all cases represented by a brown color, which means that L-band (red) offers the best separability, followed closely by C-band (green) and distantly by X-band (blue). It can be noticed that C-band is stronger in greenish cells, such as the forest-residential pair. In these examples the green color is not very strong due to the fact that L- and X-band are also contributing, but C-band is prevalent enough to show these cells in a greenish hue.

## 2) Land Cover Classification With Intensity Images:

### a) Land cover classification with seven images per band:

The first classification experiments correspond to the same datasets employed in the separability analysis, i.e., using seven dates at each frequency band, and using the intensity of the two available polarimetric channels at each date. With this decimation of the C- and X-band datasets we consider an equitable scenario for assessing the contribution of the three frequency bands, as each frequency band is providing the same amount of images as input features for the classifier.

The overall accuracy is shown in Table III for combinations of all frequency bands. When only one frequency band is employed, the best OA is for L-band with 81%, closely followed by C-band, whereas X-band reaches only 70%. Regarding the pairs of frequency bands, the two cases with L-band offer very similar OA (around 85%), which manifests the complementarity of L-band with respect to the other two bands. Combining C- and X-band the OA is below 82%, but it improves with respect

TABLE IV  
F1-SCORE OBTAINED FOR LAND COVER WITH SEVEN IMAGES PER FREQUENCY BAND

Bands	Rice	Water	Fruit tree	Forest	Olive grove	Arable land	Urban	Residential
L	92.22	79.78	60.03	74.43	74.30	77.16	80.33	37.28
C	92.11	87.83	53.25	73.50	62.01	70.16	81.89	40.18
X	90.33	83.46	41.45	59.45	55.20	61.59	62.54	15.05
L & C	93.29	91.90	69.58	81.49	77.12	79.41	85.96	55.65
L & X	92.98	91.19	66.29	82.33	79.09	79.21	82.74	52.73
C & X	92.70	93.44	60.04	79.95	69.05	72.64	83.86	52.06
L & C & X	93.12	94.06	72.41	85.66	80.11	79.71	86.97	64.51

TABLE V  
OVERALL ACCURACY OBTAINED FOR LAND COVER WITH 20 IMAGES AT C- AND X-BAND

Bands	OA	$\sigma$
C	84.56	1.23
X	77.62	1.43
C & X	86.22	1.35

to any of the two bands alone. Finally, the joint usage of the three bands provides the best result, with an OA above 86%.

For the same combinations, the F1-score is also evaluated. It is shown in Table IV, where the particular accuracy for each class is displayed. For most classes, the highest F1-score is found at L-band. In this frequency, arable land (77.16%), olive grove (74.30%), and fruit tree (69.03%) obtain higher accuracies than their counterparts at C-band. On the contrary, C-band provides greater F1-score than L-band for classes, such as water (87.83%) and urban (81.89%). As far as X-band is concerned, this frequency obtains the lowest accuracies when used alone. Only in classes, such as rice (90.33%) and water (83.46%), the accuracy is similar to the other individual bands.

With dual-band frequency combinations, we obtain mixed results. L- and C-band provide the best F1-score in 5 out of 8 classes. The three classes with different behavior correspond to water, forest, and olive grove. Water stands out above all combinations in the C- and X-band case (93.44%), whilst forest and olive grove obtain the best scores among dual-band cases in the combination of L- and X-band, with F1-scores of 82.33% and 79.09%, respectively.

When the three bands are combined in the same classification process, the accuracy for each class is maximized to its highest value among the whole set of combinations. The most noticeable case is residential zone, the class with lowest F1-score, for which the combination of the three bands achieves 64%, i.e., a 9–12% improvement with respect to the combinations of two bands. There is also an improvement of 3% with the use of the three bands for fruit tree and forest classes over the best of the other cases (individual bands and pairs of bands).

b) Land cover classification with 20 intensity images at C- and X-band: In this case an equitable analysis using only C- and X-band is intended. As the X-band dataset is made up of 20 images, a decimation process is applied over the C-band dataset so as to match the time sampling of the X-band dataset. Therefore, in this case a set of 20 dual-pol images for each frequency band is employed at the input of the classifier. The classification scores are shown in Tables V and VI.

The increase in the number of images with respect to the previous experiment entails an improvement in the overall accuracy

TABLE VI  
F1-SCORE OBTAINED FOR LAND COVER WITH 20 IMAGES AT C- AND X-BAND

Bands	Rice	Water	Fruit tree	Forest	Olive grove	Arable land	Urban	Residential
C	94.17	92.86	67.85	82.54	72.45	77.69	83.75	50.15
X	93.17	85.74	53.13	68.55	65.03	71.09	65.60	21.55
C & X	93.84	95.36	71.34	86.69	77.62	78.36	85.72	61.49

TABLE VII  
OVERALL ACCURACY OBTAINED FOR LAND COVER WITH ALL AVAILABLE IMAGES AT ALL BANDS

Bands	OA	$\sigma$
L	81.41	1.35
C	86.71	1.24
X	77.61	1.47
L & C	88.01	1.38
L & X	86.61	1.35
C & X	87.75	1.25
L & C & X	89.03	1.20

produced by the individual bands of about 6–7%. Moreover, the merge of C- and X-band provides an OA almost equal to the maximum value obtained with the combination of the three bands (using seven images per band), i.e., above 86%.

Regarding the F1-scores, C-band always gets better accuracies than X-band for all the land cover classes assessed, with differences ranging from 1% for rice to 29% for residential zones. Then, when both bands are combined all classes but rice obtain F1-scores higher than with C-band alone. Residential zones and olive grove display a remarkable improvement in the combined experiment when compared to the same results achieved at C-band. Their C-band F1-score is 50.15 and 72.45%, respectively, whereas the joint use of C- and X-band provides an accuracy of 61.49% and 77.62%, respectively.

*c) Land cover classification with all intensity images at all bands:* The last experiment carried out by considering only backscatter data consists of using all the available images, i.e., 7 at L-band, 61 at C-band, and 20 at X-band. Since the number of images is different for each band, this test is not about comparing the results of the three frequency bands, but about maximizing the accuracy by using all available intensity images.

The overall accuracies are shown in Table VII. The overall conclusion is that, thanks to the much larger number of images (one acquired every six days during the whole year), the C-band dataset achieves an accuracy (86.71%) better than L-band (81.41%) and X-band (77.61%).

When merging frequency bands, the improvement with respect to C-band alone is small (1–2%). In fact, the combination of the L- and X-band datasets produces the same score as C-band alone (with a negligible 0.1% difference). In any case, the fusion of the three datasets bands improves the final OA over all the previous cases, reaching 89%.

The behavior is also similar, with a few exceptions, for the F1-scores, which are shown in Table VIII. First, the accuracy for each class, when using only the C-band, is the highest obtained out of the three individual bands. Then, L-band gets better F1-scores than X-band in six out of eight classes. This is noteworthy, as in these tests the L-band dataset is composed of only seven images, whilst the X-band dataset is composed of 20 images. Therefore, with this dataset L-band performs better than

TABLE VIII  
F1-SCORE OBTAINED FOR LAND COVER WITH ALL AVAILABLE IMAGES AT ALL BANDS

Bands	Rice	Water	Fruit tree	Forest	Olive grove	Arable land	Urban	Residential
L	92.22	79.78	59.97	74.37	74.38	77.22	80.28	37.31
C	94.44	95.03	74.29	84.15	76.41	81.46	85.74	56.44
X	93.17	85.66	53.04	68.53	65.07	71.12	65.61	21.52
L & C	94.16	94.66	77.21	86.00	81.51	82.80	87.76	64.06
L & X	93.54	92.69	71.11	85.07	81.34	81.05	83.08	54.82
C & X	93.82	95.74	75.88	87.85	80.99	81.47	87.07	65.24
L & C & X	93.78	95.70	79.95	89.59	84.76	82.88	88.53	71.25

TABLE IX  
OVERALL ACCURACY OBTAINED FOR LAND COVER WITH 16 COHERENCES AT C- AND X-BAND

Bands	OA	$\sigma$
C	72.89	1.60
X	62.42	1.55
C & X	74.88	1.80

TABLE X  
F1-SCORE OBTAINED FOR LAND COVER WITH 16 COHERENCES AT C- AND X-BAND

Bands	Rice	Water	Fruit tree	Forest	Olive grove	Arable land	Urban	Residential
C	89.62	69.71	48.57	57.94	59.98	64.88	83.28	41.20
X	87.64	44.11	26.06	45.48	48.17	52.57	69.02	18.62
C & X	92.13	65.70	52.11	61.36	63.05	64.77	84.94	47.54

X-band to separate general land cover classes. As for the dual frequency cases, L- and X-band results are the worst compared with those obtained in the L- and C-band and C- and X-band cases. Nevertheless, the highest F1-scores are obtained by the fusion of L-, C-, and X-band data for six out of eight classes, i.e., all but rice and water.

*3) Land Cover Classification With Repeat-Pass Coherence:* The performance of repeat-pass coherence for land cover classification is studied in this section. L-band data are not used because the available temporal baselines are very long and irregular. Therefore, the analysis is focused on C- and X-band.

*a) Land cover classification with 16 coherences at C- and X-band:* As in the case of the intensity images, in order to study the contribution of the frequency band by avoiding the influence of the amount of acquisitions, we limit in a first experiment the available C-band coherence images (60 in total) to match the number and dates of the X-band dataset (16 coherence images). For this purpose, the C-band six-day coherences which are inside the time interval of the 11-day X-band coherences are selected, leaving only one in case two of them are present. The classification scores obtained with the two sets of 16 coherence images are shown in Tables IX and X.

The time series of coherence perform worse than the intensity images (see Section III-A2b), but the relative behavior of the independent band is the same: the OA provided by C-band is 10% better than that of X-band. Moreover, there is some complementarity between the bands, since the fusion of both bands provides a 2% improvement in OA with respect to C-band alone.

The overall prevalence of C-band over X-band is more pronounced for individual classes. For seven classes out of eight (all but rice), the F1-score obtained at C-band is 10% or more greater than at X-band. The most extreme examples are water and residential zones, with differences greater than 20%.



TABLE XI  
OVERALL ACCURACY OBTAINED FOR LAND COVER WITH ALL COHERENCES AT C- AND X-BAND

Bands	OA	$\sigma$
C	84.98	1.05
X	62.42	1.53
C & X	83.29	0.89

TABLE XII  
F1-SCORE OBTAINED FOR LAND COVER WITH ALL COHERENCES AT C- AND X-BAND

Bands	Rice	Water	Fruit tree	Forest	Olive grove	Arable land	Urban	Residential
C	93.46	88.90	70.22	83.06	76.46	77.69	86.06	57.72
X	87.69	44.19	26.03	45.63	48.18	52.53	68.93	18.62
C & X	93.41	80.94	67.48	82.33	74.33	73.05	86.52	57.52

TABLE XIII  
OVERALL ACCURACY OBTAINED FOR LAND COVER WITH 16 INTENSITY IMAGES AND 16 COHERENCE IMAGES AT C- AND X-BAND

Bands	OA	$\sigma$
C	86.40	1.19
X	80.60	1.24
C & X	87.96	1.06

TABLE XIV  
F1-SCORE OBTAINED FOR LAND COVER WITH 16 IMAGES AND 16 COHERENCES AT C- AND X-BAND

Bands	Rice	Water	Fruit tree	Forest	Olive grove	Arable land	Urban	Residential
C	93.99	93.47	75.98	85.30	77.50	78.99	85.94	63.33
X	94.25	86.75	64.72	70.65	67.38	75.11	72.79	30.40
C & X	94.37	95.39	78.36	87.65	80.60	80.87	88.03	72.17

On the other hand, in the C- and X-band case all classes but water and arable land get better F1-scores than their counterparts in the C-band only. This predominance of C-band over X-band in all the accuracy metrics obtained in this experiment is expected for two reasons. First, the temporal baseline employed in the computation of the coherence is longer at X-band than at C-band (11 days versus 6 days). Second, radar images acquired at short wavelengths (X-band) are known to decorrelate faster than at longer ones (C-band) over natural areas and vegetation [35]. Therefore, the time series of X-band coherence are noisier and present a lower dynamic range than at C-band. In addition, the coarser temporal resolution of the X-band data does not allow separating changes produced within a 11-day interval, whereas at C-band the six-day sampling enables locating them better in the time coordinate, hence favoring the classification if these changes are characteristic of the classes.

*b) Land cover classification with all C- and X-band coherences:* In this section, all the repeat-pass interferometric coherences are considered as input data for the classifier. Therefore, the C-band dataset is made up of 60 coherence images per polarimetric channel, computed every 6 days, whereas the X-band dataset is composed of 16 interferometric coherence images per polarimetric channel and computed every 11 days. Classification results in terms of OA and F1-score are shown in Tables XI and XII.

In this case, the C-band coherence dataset alone produces an OA close to 85%, which is almost the one obtained by the set of all C-band intensity images (86.71% in Table VII). Notably, the

TABLE XV  
OVERALL ACCURACY OBTAINED FOR LAND COVER WITH ALL IMAGES AND ALL COHERENCES AT C- AND X-BAND

Bands	OA	$\sigma$
C	89.33	0.99
X	81.38	1.24
C & X	89.92	1.04

TABLE XVI  
F1-SCORE OBTAINED FOR LAND COVER WITH ALL IMAGES AND ALL COHERENCES AT C- AND X-BAND

Bands	Rice	Water	Fruit tree	Forest	Olive grove	Arable land	Urban	Residential
C	94.32	96.50	80.43	90.73	84.64	82.19	87.39	68.91
X	94.28	87.22	65.74	72.74	69.11	75.75	72.84	31.69
C & X	94.43	96.51	81.53	91.19	85.38	82.99	88.92	75.10

TABLE XVII  
OVERALL ACCURACY OBTAINED FOR CROP TYPE WITH SEVEN IMAGES PER FREQUENCY BAND

Bands	OA	$\sigma$
L	70.80	0.73
C	78.22	0.75
X	64.50	0.91
L & C	86.41	0.67
L & X	85.87	0.51
C & X	85.45	0.58
L & C & X	90.35	0.52

fusion with the X-band coherence dataset does not improve the OA, but degrades it by more than 1%. It must be noted that the repeat-pass coherence at X-band is generally much lower than at C-band because of two factors: 1) wavelength and 2) temporal baseline. Higher frequencies exhibit faster decorrelation rates due to the interaction with smaller (and more variable) elements in the scene. Moreover, the X-band temporal baseline is 11 days, almost twice the one available at C-band (six days). As a result, coherence is very low, and noisy due to its limited estimation, at X-band for most classes. Therefore, the results obtained by the X-band data alone are very poor, and, consequently, they also degrade the combined performance with C-band.

By inspecting the F1-scores, the difference between the results of both frequency bands follows the same trend for all classes. In particular, only for rice, forest, urban, and residential zones the combination of both bands does not degrade much the performance with respect to C-band alone, but for the other classes the difference is more noticeable.

*4) Land Cover Classification With Intensity and Coherence Images:* In the last tests, both intensity and coherence images are employed as input features to the classifier.

*a) Land cover classification with 16 intensity and 16 coherence images at C- and X-band:* The initial addition of the intensity and the coherence is performed in an equitable way, as only those images which match the first date in the computation of each interferometric coherence are selected, and they are restricted to the number of dates of X-band, i.e., 16 dates. Therefore the datasets for each frequency band are made up of 16 interferometric coherences plus 16 intensities for each polarimetric channel. The accuracy metrics obtained are shown in Tables XIII and XIV.

TABLE XVIII  
F1-SCORE OBTAINED FOR CROP TYPE WITH SEVEN IMAGES PER FREQUENCY BAND

Bands	Wheat	Maize	Fallow	Sunflower	Chickpea	Alfalfa	Rice	Cotton	Sugar beet	Potato	Sweet potato	Pepper	Onion	Carrot	Pumpkin	Tomato	Quinoa
L	53.95	41.72	11.59	42.33	14.30	53.62	89.09	85.61	73.02	32.32	43.16	43.43	32.16	54.70	51.94	76.09	25.99
C	75.44	68.82	25.79	49.61	12.36	54.18	80.17	90.75	83.77	48.24	28.94	21.03	40.08	46.85	28.14	83.95	44.98
X	82.35	54.81	16.25	67.08	9.98	51.95	92.78	78.03	70.16	16.50	22.21	9.54	22.73	37.77	18.64	76.30	25.97
L & C	80.60	78.01	31.85	64.31	39.67	72.54	96.30	94.80	87.34	53.53	59.55	56.27	50.71	66.63	59.91	88.95	56.86
L & X	88.27	73.24	29.27	74.82	34.31	73.29	98.96	94.31	85.75	37.51	64.53	56.30	45.91	71.03	68.74	89.02	49.57
C & X	88.41	79.27	32.84	73.77	31.59	70.77	97.95	92.61	88.37	47.93	44.39	30.38	53.02	65.80	42.36	92.02	52.43
L & C & X	90.78	84.60	38.78	79.27	53.67	80.32	99.09	95.86	90.75	53.71	72.01	65.71	59.11	76.40	71.71	93.30	65.19

TABLE XIX  
OVERALL ACCURACY OBTAINED FOR CROP TYPE WITH 20 IMAGES AT C- AND X-BAND

Bands	OA	$\sigma$
C	88.13	0.56
X	80.89	0.96
C & X	91.87	0.53

The overall accuracy for the three cases considered is quite high, i.e., above 80%, which evidences the complementarity of the sensitivity to scene properties provided by backscatter (intensity) and interferometry (coherence). As in previous examples, C-band performs better than X-band. In addition, in the merged case, i.e., C- and X-band, the final accuracy improves by 2% to reach almost 88%.

The class-specific accuracies are also high when observing the F1-scores. C-band provided better results than X-band, with the exception of rice (93.99%) in which its score is better at X-band (94.25%). Once again, there is a noticeable difference between the F1-scores of residential at C- and X-band (63% versus 30%), but there is also complementarity, since the merged result improves up to an F1-score equal to 72%.

*b) Land cover classification with all intensity and coherence images at C- and X-band:* For this final classification test, we make use of all the intensities and coherences available in both X and C-band. This means that, for each polarization channel, 61 intensity and 60 coherence images will be used at C-band, whilst the X-band dataset is composed of 20 intensity images and 16 interferometric coherence images.

Results in Table XV show that, by using all the features available at the two bands, the OA score reaches almost 90%. In fact, C-band alone provides almost the same maximum OA (89.33%), which is much better than the accuracy provided by X-band (81.38%).

In this test, the C-band dataset comprises 61 images and 60 coherences, whereas the X-band dataset includes 20 images and 16 coherences. Consequently, the C-band dataset is by far more complete than the X-band dataset in terms of number of features and observation period, hence producing this excellent performance alone. The combined classifier, which exploits the product-of-experts concept, relies on the C-band results, which are much better than the X-band ones. However, it must be noted that, contrarily to Section III-A3b, in this case the OA of the combination of C- and X-band is slightly better than C-band alone. This means that X-band provides some extra information not found in the C-band data.

The F1-scores are shown in Table XVI. By comparing both individual frequency bands, C-band obtains better accuracies in all the classes assessed. In fact, except residential zones (68.91%)

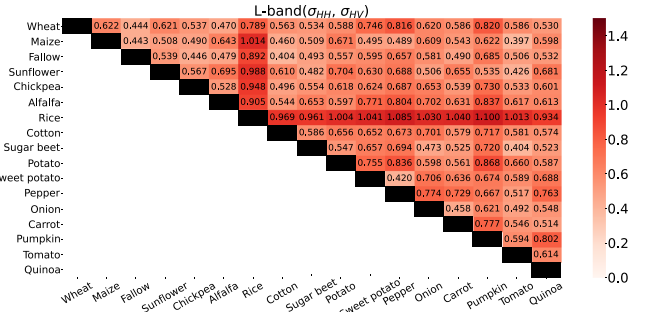


Fig. 13. Separability matrix for crop type at L-band.

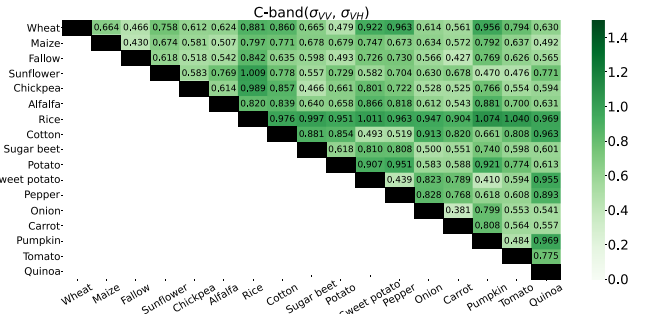


Fig. 14. Separability matrix for crop type at C-band.

all the F1-scores are above 80%, with water (96.50%) and rice (94.32%) as the ones reaching the highest scores of the whole set. Importantly, the scores of all classes are maximized when using C- and X-band together. It is not a great improvement with respect to the accuracy obtained with C-band alone, nonetheless it is consistent for all classes.

## B. Crop-Type Mapping

The results for crop classification are presented in this section following the same tests employed for land cover classification in the previous section.

*1) Separability Analysis:* As with the land cover case, the JM distances are computed for each possible pair of crop classes by using as input data the intensity time series, limited to seven dates, of each frequency band: HH + HV for L-band, VV + VH for C-band, and HH + VV for X-band.

The L-band separability matrix is displayed in Fig. 13. In general, the JM distances are smaller than for the land cover case. The values obtained for this band are not very high, ranging from 0.4 to 1.1. Among all crop types, rice is highlighted as the class with the highest separability between it and the rest of crops. In fact, it is the only class with values greater than 0.9. Apart from rice, there are specific crop pairs with JM distances

TABLE XX  
F1-SCORE OBTAINED FOR CROP TYPE WITH 20 IMAGES AT C- AND X-BAND

Bands	Wheat	Maize	Fallow	Sunflower	Chickpea	Alfalfa	Rice	Cotton	Sugar beet	Potato	Sweet potato	Pepper	Onion	Carrot	Pumpkin	Tomato	Quinoa
C	88.02	79.21	38.89	78.49	45.86	77.20	98.41	93.41	94.46	58.48	51.55	33.93	66.60	65.75	50.08	91.91	68.00
X	90.16	74.85	25.44	85.93	25.56	71.02	99.42	89.10	89.04	36.28	34.71	21.73	49.13	61.32	42.05	84.99	51.66
C & X	93.67	88.30	44.49	89.16	58.45	83.27	99.82	94.90	96.23	58.66	65.96	49.51	79.21	80.74	63.23	95.08	76.36

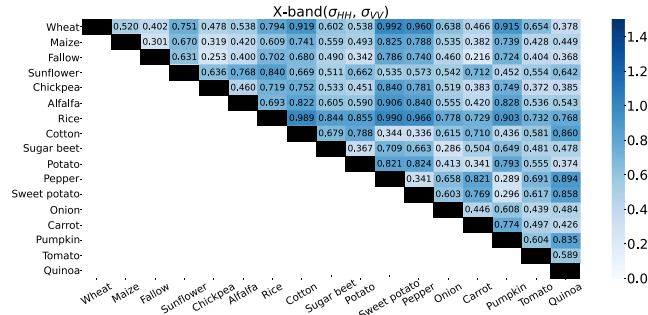


Fig. 15. Separability matrix for crop type at X-band.

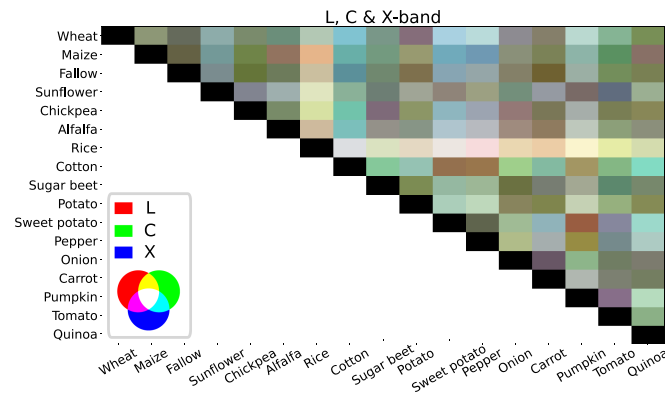


Fig. 16. Joint RGB representation of the three separability matrices obtained for crop type at L-band (red), C-band (green), and X-band (blue).

above 0.8, like those formed by pairs of potato, pepper, wheat, and pumpkin.

The JM distances computed for C-band are shown in Fig. 14. Compared to L-band, the main range of values is the same, i.e., between 0.4 and 1.1. Although rice is also the most separable class with respect to the rest, at C-band there are many more cases than at L-band of crop pairs showing JM distance values above 0.8. Some pairs with values above 0.9 are sweet potato versus wheat (0.922), pepper versus potato (0.954), and quinoa versus cotton (0.963). Therefore, the overall separability is better at C-band than at L-band.

The pairwise separability measured at X-band is depicted in Fig. 15. At this frequency, no pair presents a JM distance above 1, and we can find combinations of crops with values below 0.3, e.g., sugar beet versus onion (0.286), pepper versus pumpkin (0.296), and carrot versus fallow (0.216). Therefore, the overall separability provided by X-band is worse than that provided by L- and C-band.

As a combined comparative analysis we show in Fig. 16 the color composite of the three separability matrices, in which L-, C-, and X-band are represented by red, green, and blue colors, respectively. The first comment is obvious: there are

TABLE XXI  
OVERALL ACCURACY OBTAINED FOR CROP TYPE WITH ALL AVAILABLE IMAGES AT ALL BANDS

Bands	OA	$\sigma$
L	70.81	0.69
C	90.43	0.47
X	80.90	0.97
L & C	90.55	0.53
L & X	89.67	0.57
C & X	92.58	0.52
L & C & X	93.34	0.55

plenty of different colors in this representation, which means that there exist complementarity among the three bands for separating crop classes. Some pairs appear represented mostly in primary colors, for which one of the bands provides much better separability than the others. For instance, wheat versus cotton and maize versus sweet potato exhibit a blue color because they are best separated at X-band. Maize and tomato are best separated at C-band (shown in green color), whereas maize and quinoa are best separated at L-band (shown in reddish color). In other cases, secondary colors (i.e., addition of two primary colors) are observed. For instance, carrot and fallow are better separated at L- and C-band than at X-band, but with much lower separability, so it is shown in brown (result of low values of red and green). Finally, a few pairs show high JM distance for the three frequency bands. We can highlight the rice pairs as the ones which are the closest. For instance, rice versus cotton is depicted in a light color because they are very separable in the three bands.

2) Crop Classification With Intensity Images:

a) Crop classification with seven images per band: The classification scores, OA and F1-score, obtained using seven dual-pol intensity images per band are shown in Tables XVII and XVIII, respectively. Regarding the OA, as it could be anticipated from the separability matrices, the individual frequency band with best performance is C-band (78%) followed by L-band (70%) and then X-band (64%). The most interesting results are obtained when combining these bands, either in pairs or all three together.

When combined, the best two bands, L and C, improve significantly the final OA. The fusion of their results makes the accuracy reach 86%, despite their individual values were 70% and 78%. More notably, the other two combinations, L- and X-band, and C- and X-band, are not far from this result as both get OA values above 85%, which is quite remarkable taking into account the much lower accuracy of each individual frequency band. Finally, the overall best OA is obtained when the three frequency bands are merged, yielding an OA above 90%. This maximum score is the result of the complementarity of the information provided by the three frequency bands taking



TABLE XXII  
F1-SCORE OBTAINED FOR CROP TYPE WITH ALL AVAILABLE IMAGES AT ALL BANDS

Bands	Wheat	Maize	Fallow	Sunflower	Chickpea	Alfalfa	Rice	Cotton	Sugar beet	Potato	Sweet potato	Pepper	Onion	Carrot	Pumpkin	Tomato	Quinoa
L	53.94	41.79	11.77	42.44	14.30	53.69	89.16	85.66	72.94	32.39	42.87	43.47	32.00	54.43	51.93	76.05	26.16
C	89.89	81.39	44.12	82.12	46.81	80.17	98.67	94.55	94.83	62.99	59.74	41.36	70.89	72.70	58.57	93.66	78.54
X	90.19	74.85	25.51	85.92	25.46	71.11	99.41	89.08	89.09	36.35	34.52	21.67	49.29	61.25	41.98	85.03	51.60
L & C	88.38	81.27	39.34	79.37	55.04	80.71	99.33	95.29	94.28	59.26	66.81	63.07	61.92	74.35	72.99	92.85	71.49
L & X	91.79	81.37	35.95	86.04	52.61	78.70	99.81	95.28	91.87	49.61	69.11	61.67	58.58	76.87	79.41	91.26	66.87
C & X	93.76	88.65	45.98	89.35	59.45	83.40	99.81	95.39	96.32	61.26	71.25	53.08	80.68	81.62	69.12	95.54	79.84
L & C & X	93.98	88.84	47.68	89.46	67.84	85.02	99.89	96.27	95.93	61.37	78.77	71.55	73.95	82.64	84.24	95.29	81.62

TABLE XXIII  
OVERALL ACCURACY OBTAINED FOR CROP TYPE WITH 16 COHERENCES  
AT C- AND X-BAND

Bands	OA	$\sigma$
C	70.54	1
X	56.90	0.86
C & X	72.81	0.80

into account their wavelengths and, hence, their sensitivity to different aspects of the plants and the ground.

The commented general improvement resulting from the combination of bands can be interpreted by attending to the crop classes which are specifically benefited by this frequency diversity. For this purpose, the F1-scores are displayed in Table XVIII. When using the frequency bands in an individual basis, C-band gets the highest F1-score in 9 out of 17 classes, followed by L-band (5 classes), and X-band (3 classes). The different performance of the bands produces some extreme cases. For instance, in the case of wheat, the X-band score is 82% whilst at C- and L-band it is 75% and 54%, respectively, i.e., there is a dynamic range close to 30%. In a reverse way, the F1-score of pepper and pumpkin ranges from 9 and 18% at X-band to 43 and 52% at L-band. For quinoa and maize the F1-score is around 15% better at C-band than at the other two frequencies.

The physical reasons of the better classification performance of one band with respect to the others are due to multiple factors. One of them is the sensitivity of the frequency band to the plant morphology and the different interaction provided by the operating wavelength. For instance, wheat, rice, and sunflower crops are characterized by a vertical structure, high plantation density, and not so tall plants (up to 1 m). As a result, X-band enhances the scattering from the top canopy of these crops better than other bands whose response is more affected by the lower plant parts and the soil [36], [37], [38]. At the other extreme, pumpkin and pepper exhibit big wide leaves which make them better suited to longer frequencies (i.e., L-band). In between, quinoa and maize, with taller plants and not so dense plantations, are better separated from the rest at C-band, which offers a balanced response from the vegetation and the soil [39]. Both the canopy geometrical structure and the dielectric properties of the elements in the scene (leaves, branches, fruits, stems, and soil) have an impact on the radar response obtained at different frequencies. The vertical distribution of scattering properties of different crops has been studied in the past using 1-D profiles in laboratory experiments [40] and SAR tomography with airborne data [41]. Finally, and constituting a key asset for crop classification, all the aforementioned physical properties of the crops change with time along the growing season. Consequently,

the usage for classification of multitemporal datasets exploits the crop calendar, which is crop-specific over the same geographical region [24]. At any acquisition date, the growth status of the different crops affects the separability between classes at different frequency bands, and the change of crop features may favor one band or another. This includes the soil properties (e.g. moisture and roughness), which constitute an important contribution of the radar backscatter for most crops, and whose response and relative weight in the radar echo strongly depend on the wavelength [42].

In the merged classifications formed by two frequency bands, there are clear enhancements with respect to the individual bands. In some cases, like for chickpea and alfalfa, the merged accuracy is 20% better than any of the individual bands. On the other hand, most of the resulting F1-scores are quite similar for the three combinations, offering values within a 10% interval for each crop type. The most noticeable exceptions are sweet potato, pepper, and pumpkin, for which the combination of C- and X-band is worse than the other two (up to 20–25% below them). All of them are broadleaved crops, hence they are better characterized with longer wavelengths.

In the end, the best classification performance is obtained for all classes when using together the three frequency bands. The accuracy especially improves with respect to the best of the combinations of two bands for classes, such as chickpea (+14%), pepper (+9%), quinoa (+9%), and sweet potato (+8%). The only case with an improvement smaller than 1% is potato, for which the addition of X-band does not improve much in comparison with L- and C-band combined.

*b) Crop classification with 20 intensity images at C- and X-band:* In this second experiment, we focus only on C- and X-band but increasing the length of the time series, using 20 acquisitions in both cases. The achieved OA values are shown in Table XIX. As in the case of seven images, C-band provides better OA than X-band, but now the difference is smaller than with seven images (8% instead of 14%). The accuracy has increased in all cases (individual bands and combination), reaching almost 92% with the C- and X-band fusion. In fact, this score is better than the previous result with all the three bands using seven images. The improved performance is the result of becoming more sensitive to the changes produced in the crops along the year, since they are mainly due to their crop calendar, i.e., specific of each crop type. With 20 acquisition dates along the year, instead of only seven, it is possible to catch sudden events, like harvest, and also to observe the crops in different phenological stages, which clearly helps separate them in the classifier.

Regarding the F1-scores, which are presented in Table XX, it can be observed that C-band performs better than X-band for all

TABLE XXIV  
F1-SCORE OBTAINED FOR CROP TYPE WITH 16 COHERENCES AT C- AND X-BAND

Bands	Wheat	Maize	Fallow	Sunflower	Chickpea	Alfalfa	Rice	Cotton	Sugar beet	Potato	Sweet potato	Pepper	Onion	Carrot	Pumpkin	Tomato	Quinoa
C	68.07	53.26	51.07	42.74	24.27	47.95	72.66	83.96	86.25	9.93	18.69	10.06	28.36	45.39	13.92	72.08	37.30
X	44.61	40.51	61.02	33.33	10.62	34.05	54.70	76.63	72.40	12.54	17.39	5.25	20.31	30.36	8.44	61.68	25.38
C & X	68.15	55.64	65.75	47.27	27.58	49.66	83.90	85.77	87.35	15.68	23.90	11.14	33.05	47.48	14.65	75.54	40.59

TABLE XXV  
OVERALL ACCURACY OBTAINED FOR CROP TYPE WITH ALL COHERENCES  
AT C- AND X-BAND

Bands	OA	$\sigma$
C	83.97	0.66
X	56.84	0.89
C & X	81.19	0.58

crop types but wheat, rice, and sunflower. Notably, the fusion of C- and X-band shows better accuracy than the individual bands for all crop types. In some cases, the improvement with respect to the best individual band is very clear, such as for pepper, sweet potato, carrot, sweet potato, chickpea, and pumpkin, for which the accuracy increase is greater than 10%.

*c) Crop classification with all intensity images at all bands:* In this test, all the intensity images available at all bands are used in the classification process. The resulting values of OA are shown in Table XXI.

Regarding the use of individual bands alone, we found in the seven-image test that C-band provided the best results, followed in order by L- and X-band. However, in this test the order of L- and X-band is reversed: X-band outperforms L-band. The reason is the larger number of images (20 instead of 7) for X-band, which is beneficial for the identification of the crop calendar and, hence, to distinguish among classes.

It is also important to note that C-band alone reaches an OA of 90%, very close to the maximum OA values found so far. This is a consequence of the very rich time sampling of Sentinel-1, which provides 61 images regularly arranged along the whole year. In fact, the addition of L-band to C-band does not really improve the results. Moreover, the combined use of the other two bands, L and X, obtains an OA lower than C-band alone. In contrast, the fusion of C-band with X-band provides a 2% improvement with respect to C-band alone. Finally, the best overall score corresponds to the use of the three bands, with an OA of 93.34%, which is the best result of all the tests analyzed so far.

As for the accuracy of the individual crops, Table XXII shows the F1-score of all band combinations. In the cases corresponding to individual bands, C-band outperforms the other bands in all crop types except for wheat, sunflower, and rice, which are better classified at X-band, and for pepper, which is better classified at L-band despite the dataset having comprised only seven images.

Among the combinations of two frequency bands, the best F1-score is provided by C- and X-band for all crops but for pepper, which is improved by the two L-band combinations, and pumpkin, for which the combination of L- and X-band is clearly the best case.

Finally, the merged result with three bands offers the best accuracy for 14 out of 17 crops. The exceptions correspond to sugar

beet, onion, and tomato. The L-band dataset performs worse than other bands in this experiment due to the small number of images (7 instead of 20 and 61), which limits its sensitivity to the crop calendar because of an insufficient temporal sampling. The most noticeable contribution of the combination of the three bands with respect to two bands is found for pepper (+10%), chickpea (+8%), sweet potato (+7%), and pumpkin (+5%).

*3) Crop Classification With Repeat-Pass Coherence:* The performance of repeat-pass coherence for crop classification is studied in this section. L-band data are not used because the available temporal baselines are very long and irregular. Therefore, the analysis is focused on C- and X-band.

*a) Crop classification with 16 coherences at C- and X-band:* The OA values obtained with the same number of coherence images (16) for both bands are shown in Table XXIII. The accuracy is lower than the one obtained with the intensity images. In this case, C-band is clearly much better than X-band, since it provides an accuracy improvement of 14%. As it was discussed for the land cover case, it must be recalled that the X-band coherence is measured with an 11-day temporal baseline, whereas the C-band coherence is obtained with a temporal baseline of six days. The increased temporal baseline produces more decorrelation over vegetated areas, hence reducing the dynamic range of the X-band dataset, which contributes less to crop classification purposes. Anyway, for this test the best OA is achieved by the joint use of C- and X-band (72.81%) which improves the performance obtained by any of the two bands alone.

In agreement with the overall accuracy, the F1-scores obtained for each crop type, which are listed in Table XXIV, are higher at C-band than at X-band in all cases but in one (potato). The maximum difference is found for wheat, whose C-band F1-score is 24% higher than at X-band. Regarding the fusion of both bands, the scores are only slightly better (less than 5%) than the ones provided by the C-band alone. The exception to this behavior is rice, for which the merged accuracy reaches almost 84% although the individual ones were 72% and 54% at C- and X-band, respectively.

*b) Crop classification with all C- and X-band coherences:* This test corresponds to the scenario in which all the coherence values are used as input features of the classifier: 60 at C-band and 16 at X-band. The OA is shown in Table XXV. In comparison to the previous test, the performance of C-band alone is greatly improved, reaching an OA above 84%, instead of 70%. This performance enhancement is a direct consequence of the one-year length of the time series and the fact that all possible six-day coherence values are available. Thanks to this observation scheme, all changes produced in the crops along the year are well captured, hence allowing the classifier to better distinguish among them by exploiting their different

TABLE XXVI  
F1-SCORE OBTAINED FOR CROP TYPE WITH ALL COHERENCES AT C- AND X-BAND

Bands	Wheat	Maize	Fallow	Sunflower	Chickpea	Alfalfa	Rice	Cotton	Sugar beet	Potato	Sweet potato	Pepper	Onion	Carrot	Pumpkin	Tomato	Quinoa
C	81.64	65.45	57.85	51.97	33.51	61.47	96.71	91.17	91.33	29.19	34.41	18.02	52.60	60.58	35.48	85.39	59.85
X	44.69	40.54	61.10	33.45	10.65	34.12	54.80	76.57	72.48	12.58	17.33	5.22	20.16	30.28	8.47	61.48	25.37
C & X	77.68	62.86	68.16	51.89	34.23	55.82	89.19	89.99	91.36	24.06	36.99	17.10	42.69	54.31	29.72	84.16	50.58

TABLE XXVII  
OVERALL ACCURACY OBTAINED FOR CROP TYPE WITH 16 INTENSITY IMAGES  
AND 16 COHERENCE IMAGES AT C- AND X-BAND

Bands	OA	$\sigma$
C	89.19	0.48
X	87.50	0.69
C & X	93.08	0.51

cultivation calendar and their changes along their phenological development.

In this specific example, the poor performance of the X-band classifier produces a degradation of the overall accuracy when the two datasets are merged, reducing the OA value to 81%.

When it comes to the F1-scores, listed in Table XXVI, we can appreciate that there are different behaviors in the fusion of the two bands with respect to the use of a single band. In 14 out of the 17 classes the accuracy obtained with the combination of bands (C and X) is worse than for C-band alone. The exceptions are fallow, chickpea, and sweet potato.

4) *Crop Classification With Intensity and Coherence Images:* In the last tests, both intensity and coherence images are employed as input features to the classifier.

a) *Crop classification with 16 intensity and 16 coherence images at C- and X-band:* The OA provided by the fusion of intensity and coherence, using 16 dual-pol images of each type at both bands, is illustrated in Table XXVII. The first obvious comment is on the high values obtained at the two independent bands (89.19% at C-band and 87.50% at X-band). For C-band alone this OA value is close to the 90.43% reached when using the whole time series of 60 intensity images (see Table XXI). Therefore, this demonstrates the complementarity of the information provided by interferometry with respect to backscatter, since they exhibit sensitivity to different properties of the scene. More importantly, this complementarity is more evident at X-band: the fusion of intensity and coherence improves by 7% the overall accuracy with respect to only intensity.

Regarding the combination of C- and X-band, it provides an OA above 93%, i.e., an improvement of 4% with respect to C-band alone and 6% with respect to X-band alone.

The class-specific accuracy scores are listed in Table XXVIII. The mentioned complementarity between frequency bands is obvious in these values: around half of the classes performs better at one of the two bands (10 at C-band and 7 at X-band), with a maximum difference of 10%. Then, in all classes the combination of the two bands outperforms the individual bands. The most remarkable improvements of the fusion of frequencies are obtained for pumpkin (+19%), sweet potato (+18%), pepper (+17%), chickpea (+15%), onion (+14%), and quinoa (+11%).

b) *Crop classification with all intensity and coherence images at C- and X-band:* In the final experiment, all available

intensity and coherence images of the two bands are considered. The OA values obtained are shown in Table XXIX. The result with C-band alone (91.64%) is 1% better than using only intensity and 7% better than using only coherence. As for X-band, the OA is 88.21%, that is, 7% better than using only intensity and 31% better than using only coherence. Therefore, for both bands the improvement is evident.

As for the combination of C- and X-band, it provides the best OA score of all tests, reaching 93.88%. This value is 0.5% better than the OA provided by all the intensity images of the three bands (see Table XXI) and 1.5% better than the OA provided by all the intensity images of the same two bands (see Table XXI).

Results in Table XXX show the F1-scores for all crops present in our reference data. The comments are similar to the previous test (Table XXVIII), i.e., since there is an obvious complementarity between the two bands for the employed fusion of intensity and coherence. The most noticeable increase of accuracy with respect to the results of individual bands is found for the same classes: pumpkin (+17%), pepper (+17%), chickpea (+16%), and sweet potato (+15%).

#### IV. DISCUSSION

The main objective of this work is the assessment of the contribution of time series of multifrequency SAR data in two classification domains: 1) land cover and 2) crop type. As it was previously mentioned, due to the different sensor characteristics, not only the frequency band, the datasets available enable the evaluation of time series of multiplatform SAR data in classification.

In the land cover case, a previous work of similar characteristics was conducted in [8] with a single image per band, not with time series, and the L- and C-band images were fully polarimetric. Moreover, the scene features and classes present in the area were different from this work. Consequently, a relative comparison, not an absolute one, is better suited.

In this work, we have found that the combination of intensity images at the three frequency bands (L, C, and X) increases by 5% the OA with respect to the best of the individual bands, whereas a 7% improvement was found in [8] using full-pol data. In both cases, L-band is the best individual frequency. It has to be pointed out that the use of the dual-pol intensities, HH+HV at L-band and VV+VH at C-band, yields similar values to the accuracies reported in [8], i.e., 81% at L-band and 75% at C-band, which here are 81% and 78%, respectively. However, here we are employing seven images per frequency band, not only one.

Besides this confirmation of a previous result, we have obtained other relevant results which have not been reported in the literature of land cover classification with SAR data. The first one is that adding a second band provides equivalent results



TABLE XXVIII  
F1-SCORE OBTAINED FOR CROP TYPE WITH 16 INTENSITY IMAGES AND 16 COHERENCE IMAGES AT C- AND X-BAND

Bands	Wheat	Maize	Fallow	Sunflower	Chickpea	Alfalfa	Rice	Cotton	Sugar beet	Potato	Sweet potato	Pepper	Onion	Carrot	Pumpkin	Tomato	Quinoa
C	86.77	83.74	56.76	80.27	52.66	76.29	97.98	93.91	94.57	56.14	54.83	35.45	65.64	70.42	55.02	92.12	72.07
X	91.06	80.79	65.13	87.22	42.15	70.55	99.40	91.85	95.54	54.54	43.74	26.62	63.36	74.95	57.62	91.16	70.69
C & X	93.65	89.41	66.52	89.11	67.20	81.66	99.77	95.48	96.59	60.73	72.85	52.47	79.27	82.14	76.41	95.53	83.16

TABLE XXIX  
OVERALL ACCURACY OBTAINED FOR CROP TYPE WITH ALL IMAGES AND ALL COHERENCES AT C- AND X-BAND

Bands	OA	$\sigma$
C	91.64	0.48
X	88.21	0.71
C & X	93.88	0.41

of increasing the length of the intensity time series of a single band. For instance, the OA obtained with 20 dual-pol intensity images at C-band is 84%, and it reaches 86% with 60 images. The same OA (86%) is provided by combining 20 dual-pol intensity images of C- and X-band. In the same vein, adding a third band provides equivalent results with fewer images. With our dataset, the same 86% of OA is achieved with the combination of seven dual-pol images of the three bands. In terms of total amount of images, the multifrequency set employs fewer images, so there is a compromise between availability of frequency bands (normally from multiple sensors) or availability of a long time series (from the same sensor). The relative improvement at X-band is the same (+7%) when passing from 7 to 20 intensity images. Regarding the merge of all available intensity images of all bands, it still improves the overall accuracy over the single- and dual-band tests, reaching 89%. The complementarity of information among the three bands considered has proven especially useful for some classes, like water, fruit trees, residential zones, and urban areas, for which their classification performance differs notably between frequency bands.

An original aspect of this study is the inclusion of repeat-pass interferometric coherence in the multifrequency and multitemporal framework. Despite being limited to C- and X-band, due to the data availability, we have found that the sensitivity to scene properties, and their changes along time, offers an excellent complement to the intensity data. At C-band the separate uses of all the intensity images or all the coherences get an OA around 86% in both cases, whereas their combination reaches 89%. At X-band, for which the temporal baseline is larger than at C-band, and the number of acquisition is smaller, the OA of the combination reaches 81%, in contrast to the 77% obtained with the images and the 62% obtained with the coherences alone. Then, the fusion of C- and X-band data formed by 16 pairs of images and coherences yields an OA of almost 87%, which increases to nearly 90% when all images and coherences are exploited.

Regarding crop classification, as reviewed in the Introduction, there are more examples than for land cover in the literature about the combination of multiple frequencies. In all cases the joint results improve the overall accuracy with respect to any single band, and this is also confirmed in the study presented here. Regarding the best frequency band, we found that C-band

performs better than L-band. This is in agreement with the findings published in [12], but the opposite was found in [11] and [7]. In these studies, the radar data correspond to single-date acquisitions, so the growth status of the different crops affects the separability between classes at different bands, and the change of crop features may favor one band or another.

Following the previous argument, it is then better to compare our results with those obtained with time series of images, especially because the time coordinate is a key element in crop classification due to the inherent dynamics of the scene. Unfortunately, from the multifrequency perspective, we have found only a few published studies in which multitemporal datasets acquired at different microwave frequencies are *combined*, not only *compared*. This combination was studied in [14] and [19], whereas comparisons can be found also in [13] and [16]. By using air-borne SAR data, it was found in [14] that both C- and L-band performed similarly in a multitemporal scenario, with slightly better results at C-band. Moreover, the combination of the two bands clearly improved the overall accuracy. With satellite data, the results obtained in [19] by C- and X-band data showed that with eight images per band the accuracy improved by 10% over the individual bands. Therefore, the present work is the first example of multifrequency combination in which: 1) three bands were considered (L, C, and X), 2) data were gathered by operational satellites, and 3) repeat-pass interferometric coherence was incorporated as an input feature.

With our dataset, when we restricted the acquisitions to be in the same amount for all three bands (seven dual-pol intensity images at each band), we obtained that C-band (OA 78%) performed better than L-band (OA 70%), which in turn performed better than X-band (OA 64%). When combined in pairs, all frequency pairs provided almost the same OA (85–86%), i.e., 8% better than the best band alone. And, notably, the combination of the three bands provided an OA greater than 90%. This improvement is a direct consequence of the different sensitivity provided by each frequency to the scene properties, which translates in a varying separability between classes as a function of the radar frequency. In this sense, the joint RGB representation of the pairwise separability provided by the three bands (Fig. 16) offers a clear view of the richness of the multifrequency data for this application.

Another interesting aspect is the performance when the number of images is increased, first to 20 images per band (at C and X) and then to all available (61 at C-band, 20 at X-band, and 7 at L-band). The OA provided by the 20 intensity images at C- and X-band is 91.87%, hence better than the one achieved with three frequencies using seven images per band. As a further improvement, the series of 61 C-band intensity images provides an OA equal to the test with the three bands (90.37%). Therefore, one concludes that using more bands with fewer images per band

TABLE XXX  
F1-SCORE OBTAINED FOR CROP TYPE WITH ALL IMAGES AND ALL COHERENCES AT C- AND X-BAND

Bands	Wheat	Maize	Fallow	Sunflower	Chickpea	Alfalfa	Rice	Cotton	Sugar beet	Potato	Sweet potato	Pepper	Onion	Carrot	Pumpkin	Tomato	Quinoa
C	91.88	85.90	59.25	84.13	55.44	82.12	99.16	94.79	94.96	65.25	62.64	40.08	74.03	78.66	63.05	93.94	82.60
X	91.43	81.02	65.07	87.36	42.51	72.87	99.44	92.42	95.71	55.17	49.33	28.38	65.61	75.79	59.65	91.56	71.77
C & X	94.84	89.67	67.86	89.42	71.06	84.12	99.84	95.91	96.71	65.94	77.20	57.59	83.60	85.22	80.63	95.86	86.16

is equivalent to exploiting longer time series of images from fewer frequency bands. In fact, the use of the whole time series of C-band alone, which covers the whole year with short refresh rate, produces also the same final OA (90.43%). Consequently, a tradeoff between number of bands and length of the time series is found. In any case, when we add the available images of the other two bands to the one-year long C-band dataset, the final accuracy is improved further (+3%), reaching an OA equal to 93.34%. This means that the multiple sensitivity provided by the wavelength diversity is different from the sensitivity provided by a multitemporal dataset acquired in a single frequency, and hence they both combined improve the classification performance.

This work has considered also the inclusion of repeat-pass coherence in crop classification by adding the multifrequency perspective. Examples at single frequencies were published in [24] at C-band and in [43] at X-band. In both cases, it was demonstrated that coherence and backscatter offer complementary information which help to improve classification when they are merged. This aspect is also confirmed in this work. But, more importantly, we have seen that C- and X-band are also complementary in this aspect, since the combination of 16 intensity and coherence images per band enabled the OA to reach 93%, starting from 89% and 87% obtained at C- and X-band alone, respectively. That overall accuracy is nominally the same as in the best tests.

## V. CONCLUSION

This work has served to first confirm the findings of previous studies in which multifrequency SAR data were tested for land cover classification and crop-type mapping. In the two classification domains, time series of SAR images acquired by satellite at different frequencies have been employed. In both applications, the fusion of L-, C-, and X-band data outperforms the use of only one or two bands. In second place, the exploitation of repeat-pass interferometric coherence at multiple bands has demonstrated also a contribution to enhance the classification accuracy in a multifrequency framework. Therefore, backscatter intensity and coherence offer complementary sensitivity to the scene properties, which is also frequency dependent.

A tradeoff between the length of the time series and the number of frequency bands has been found, although using all the available data (all dates and frequency bands) increases further the overall classification accuracy. Therefore, adding new images, either from the same sensor or from a different one, is beneficial in this context.

From the point of view of future systems, the next launch of L-band missions with improved revisit times and consistent acquisition schemes is expected to contribute with an additional sensitivity source. The features derived from these future sensors, both intensity and repeat-pass coherence, are expected to

enhance further the classification scores obtained in this work, in combination with the already available C- and X-band sensors and future ones.

In this work, the data available at the three frequency bands are also characterized by different sensor properties (polarimetric channels, resolution, incidence angle, etc.). Therefore, a multi-platform combination has been analyzed. If one aims at isolating the contribution of frequency from the rest of radar variables, frequency should be the only sensor parameter to change among sensors. For that purpose, specific acquisition campaigns should be designed and carried out.

## ACKNOWLEDGMENT

All the TanDEM-X data were provided by the German Aerospace Center (DLR) under project NTI-POLI6736. ALOS-2/PALSAR-2 Level 1.1 data are provided by the Japan Aerospace Exploration Agency (JAXA) under the framework of Earth Observation Research Announcement. The ALOS-2/PALSAR-2 data used in this study are property of JAXA. The reference data were kindly provided by the Regional Government of Andalucía.

## REFERENCES

- [1] S. R. Cloude, *Polarisation: Applications in Remote Sensing*. London, U.K.: Oxford Univ. Press, 2009.
- [2] J.-S. Lee and E. Pottier, *Polarimetric Radar Imaging: From Basics to Applications*. Boca Raton, FL, USA: CRC Press, 2009.
- [3] I. Hajnsek and Y.-L. Desnos, Eds., *Polarimetric Synthetic Aperture Radar. Principles and Application*. Berlin, Germany: Springer, 2021.
- [4] R. Bamler and P. Hartl, "Synthetic aperture radar interferometry," *Inverse Problems*, vol. 14, no. 4, pp. R1–R54, 1998.
- [5] P. Rosen et al., "Synthetic aperture radar interferometry," *Proc. IEEE*, vol. 88, no. 3, pp. 333–382, Mar. 2000.
- [6] D. Mandal, A. Bhattacharya, and Y. S. Rao, *Radar Remote Sensing for Crop Biophysical Parameter Estimation*. Berlin, Germany: Springer, 2021.
- [7] J.-S. Lee, M. Grunes, and E. Pottier, "Quantitative comparison of classification capability: Fully polarimetric versus dual and single-polarization SAR," *IEEE Trans. Geosci. Remote Sens.*, vol. 39, no. 11, pp. 2343–2351, Nov. 2001.
- [8] V. Turkar, R. Deo, Y. S. Rao, S. Mohan, and A. Das, "Classification accuracy of multi-frequency and multi-polarization SAR images for various land covers," *IEEE J. Sel. Topics Appl. Earth Observ. Remote Sens.*, vol. 5, no. 3, pp. 936–941, Jun. 2012.
- [9] R. Hagensieker and B. Waske, "Evaluation of multi-frequency SAR images for tropical land cover mapping," *Remote Sens.*, vol. 10, no. 2, p. 257, Feb. 2018, doi: [10.3390/rs10020257](https://doi.org/10.3390/rs10020257).
- [10] B. Guindon, P. Teillet, D. Goodenough, J. Palimaka, and A. Sieber, "Evaluation of the crop classification performance of X, L, and C-band SAR imagery," *Can. J. Remote Sens.*, vol. 10, no. 1, pp. 4–16, 1984.
- [11] K. Chen, W. Huang, D. Tsay, and F. Amar, "Classification of multi-frequency polarimetric SAR imagery using a dynamic learning neural network," *IEEE Trans. Geosci. Remote Sens.*, vol. 34, no. 3, pp. 814–820, May 1996.
- [12] D. Hoekman and M. Vissers, "A new polarimetric classification approach evaluated for agricultural crops," *IEEE Trans. Geosci. Remote Sens.*, vol. 41, no. 12, pp. 2881–2889, Dec. 2003.
- [13] D. Hoekman, M. Vissers, and T. Tran, "Unsupervised full-polarimetric SAR data segmentation as a tool for classification of agricultural areas," *IEEE J. Sel. Topics Appl. Earth Observ. Remote Sens.*, vol. 4, no. 2, pp. 402–411, Jun. 2011.

- [14] H. Skriver, "Crop classification by multitemporal C- and L-band single- and dual-polarization and fully polarimetric SAR," *IEEE Trans. Geosci. Remote Sens.*, vol. 50, no. 6, pp. 2138–2149, Jun. 2012.
- [15] A. Alonso-Gonzalez, H. Joerg, K. P. Papathanassiou, and I. Hajnsek, "Multi-frequency PolSAR change analysis for agricultural monitoring," in *Proc. 8th Int. Workshop Sci. Appl. SAR Polarimetry Polarimetric Interferometry*, Frascati, Italy, Jan. 2017.
- [16] H. Skriver et al., "Crop classification using short-revisit multitemporal SAR data," *IEEE J. Sel. Topics Appl. Earth Observ. Remote Sens.*, vol. 4, no. 2, pp. 423–431, Jun. 2011.
- [17] R. Sonobe, "Parcel-based crop classification using multi-temporal TerraSAR-X dual polarimetric data," *Remote Sens.*, vol. 11, no. 10, 2019, Art. no. 1148.
- [18] K. Jia, Q. Li, Y. Tian, B. Wu, F. Zhang, and J. Meng, "Crop classification using multi-configuration SAR data in the north China plain," *Int. J. Remote Sens.*, vol. 33, no. 1, pp. 170–183, 2012.
- [19] M. Busquier, R. Valcarce-Dineiro, J. M. Lopez-Sanchez, J. Plaza, N. Sanchez, and B. Arias-Perez, "Fusion of multi-temporal PAZ and Sentinel-1 data for crop classification," *Remote Sens.*, vol. 13, no. 19, 2021, Art. no. 3915.
- [20] T. Strozzi et al., "Landuse mapping with ERS SAR interferometry," *IEEE Trans. Geosci. Remote Sens.*, vol. 38, no. 2, pp. 766–775, Mar. 2000.
- [21] M. Engdahl and J. Hyypä, "Land-cover classification using multitemporal ERS-1/2 InSAR data," *IEEE Trans. Geosci. Remote Sens.*, vol. 41, no. 7, pp. 1620–1628, Jul. 2003.
- [22] F. Sica, A. Pulella, M. Nannini, M. Pinheiro, and P. Rizzoli, "Repeat-pass SAR interferometry for land cover classification: A methodology using Sentinel-1 short-time-series," *Remote Sens. Environ.*, vol. 232, 2019, Art. no. 111277.
- [23] A. W. Jacob et al., "Sentinel-1 InSAR coherence for land cover mapping: A comparison of multiple feature-based classifiers," *IEEE J. Sel. Topics Appl. Earth Observ. Remote Sens.*, vol. 13, pp. 535–552, 2020.
- [24] A. Mestre-Quereda, J. M. Lopez-Sanchez, F. Vicente-Guijalba, A. W. Jacob, and M. E. Engdahl, "Time-series of Sentinel-1 interferometric coherence and backscatter for crop-type mapping," *IEEE J. Sel. Topics Appl. Earth Observ. Remote Sens.*, vol. 13, pp. 4070–4084, 2020.
- [25] B. Tso and P. Mather, *Classification Methods for Remotely Sensed Data*, 2nd ed. Boca Raton, FL, USA: CRC Press, 2001.
- [26] J. A. Richards, *Feature Reduction*, Berlin, Heidelberg: Springer, 2013, pp. 343–380.
- [27] T. G. Van Niel, T. R. McVicar, and B. Datt, "On the relationship between training sample size and data dimensionality: Monte carlo analysis of broadband multi-temporal classification," *Remote Sens. Environ.*, vol. 98, no. 4, pp. 468–480, 2005.
- [28] M. Arias, M. A. Campo-Bescos, and J. Alvarez-Mozos, "Crop classification based on temporal signatures of Sentinel-1 observations over navarre province, Spain," *Remote Sens.*, vol. 12, no. 2, p. 278, Jan. 2020, doi: [10.3390/rs12020278](https://doi.org/10.3390/rs12020278).
- [29] S. Valero, L. Arnaud, M. Planells, E. Ceschia, and G. Dedieu, "Sentinel's classifier fusion system for seasonal crop mapping," in *Proc. IEEE Int. Geosci. Remote Sens. Symp.*, 2019, pp. 6243–6246.
- [30] L. Breiman, "Random forests," *Mach. Learn.*, vol. 45, pp. 5–32, 2001.
- [31] F. Pedregosa et al., "Scikit-learn: Machine learning in Python," *J. Mach. Learn. Res.*, vol. 12, pp. 2825–2830, 2011.
- [32] R. L. Lawrence, S. D. Wood, and R. L. Sheley, "Mapping invasive plants using hyperspectral imagery and Breiman Cutler classifications (random-forest)," *Remote Sens. Environ.*, vol. 100, no. 3, pp. 356–362, 2006.
- [33] S. Dey et al., "In-season crop classification using elements of the Kennaugh matrix derived from polarimetric RADARSAT-2 SAR data," *Int. J. Appl. Earth Observation Geoinformation*, vol. 88, 2020, Art. no. 102059.
- [34] S. V. Stehman, "Selecting and interpreting measures of thematic classification accuracy," *Remote Sens. Environ.*, vol. 62, no. 1, pp. 77–89, 1997.
- [35] F. Mohammadimanes, B. Salehi, M. Mahdianpari, B. Brisco, and M. Motagh, "Multi-temporal, multi-frequency, and multi-polarization coherence and SAR backscatter analysis of wetlands," *ISPRS J. Photogrammetry Remote Sens.*, vol. 142, pp. 78–93, 2018.
- [36] S. C. M. Brown, S. Quegan, K. Morrison, J. C. Bennett, and G. Cookmartin, "High-resolution measurements of scattering in wheat canopies-implications for crop parameter retrieval," *IEEE Trans. Geosci. Remote Sens.*, vol. 41, no. 7, pp. 1602–1610, Jul. 2003.
- [37] J. M. Lopez-Sanchez, S. R. Cloude, and J. D. Ballester-Berman, "Rice phenology monitoring by means of SAR polarimetry at x-band," *IEEE Trans. Geosci. Remote Sens.*, vol. 50, no. 7, pp. 2695–2709, Jul. 2012.
- [38] J. M. Lopez-Sanchez, F. Vicente-Guijalba, J. D. Ballester-Berman, and S. R. Cloude, "Polarimetric response of rice fields at C-band: Analysis and phenology retrieval," *IEEE Trans. Geosci. Remote Sens.*, vol. 52, no. 5, pp. 2977–2993, May 2014.
- [39] F. Mattia et al., "Multitemporal C-band radar measurements on wheat fields," *IEEE Trans. Geosci. Remote Sens.*, vol. 41, no. 7, pp. 1551–1560, Jul. 2003.
- [40] J. M. Lopez-Sanchez, J. Fortuny, S. R. Cloude, and A. J. Sieber, "Indoor polarimetric radar measurements on vegetation samples at L, S, C and X band," *J. Electromagn. Waves Appl.*, vol. 14, no. 2, pp. 205–231, 2000.
- [41] H. Joerg, M. Pardini, I. Hajnsek, and K. P. Papathanassiou, "3-D scattering characterization of agricultural crops at C-band using SAR tomography," *IEEE Trans. Geosci. Remote Sens.*, vol. 56, no. 7, pp. 3976–3989, Jul. 2018.
- [42] E. Ayari, Z. Kassouk, Z. Lili-Chabaane, N. Baghdadi, S. Bousbih, and M. Zribi, "Cereal crops soil parameters retrieval using L-band ALOS-2 and C-band Sentinel-1 sensors," *Remote Sens.*, vol. 13, no. 7, 2021, Art. no. 1393.
- [43] M. Busquier, J. M. Lopez-Sanchez, A. Mestre-Quereda, E. Navarro, M. P. Gonzalez-Dugo, and L. Mateos, "Exploring TanDEM-X interferometric products for crop-type mapping," *Remote Sens.*, vol. 12, no. 11, 2020, Art. no. 1774.



**Mario Busquier** (Graduate Student Member, IEEE) was born in Elda, Spain, in 1994. He received the B.Sc. degree in sound and image in telecommunication engineering and the M.Sc degree in telecommunication engineering, in 2018 and 2020, respectively, from the University of Alicante, Alicante, Spain, where he is currently working toward the Ph.D. degree in computer science with the Signals, Systems, and Telecommunications group (SST).

Since 2018, he has worked with the Signals, Systems, and Telecommunications group (SST), with which he is pursuing his Ph.D. in computer science as a pre-doctoral researcher, since 2019. His research interests include crop-type-mapping by means of radar data, SAR polarimetry and interferometry and development of scripts for automatic processing of time series of SAR SLC images.

Mr. Busquier was the recipient of the Award for Best Final Master's Project in Remote Sensing defended in Spain in 2020 of the IEEE GRSS Spanish Chapter and the "Hall of Fame" Award by the Technical University of Alicante (EPS UA), in 2022.



**Juan M. Lopez-Sanchez** (Senior Member, IEEE) was born in Alicante, Spain, in 1972. He received the ingeniero (M.S.) and doctor ingeniero (Ph.D.) degrees in telecommunication engineering from the Technical University of Valencia, Valencia, Spain, in 1996 and 2000, respectively.

From 1998 to 1999, he was a Predoctoral grantholder with the Space Applications Institute, Joint Research Centre of the European Commission, Ispra, Italy. Since 2000, he leads the Signals, Systems and Telecommunication Group, University of Alicante, Spain, where he is Full Professor, since November 2011. He has coauthored more than 100 papers in refereed journals and more than 140 papers and presentations in international conferences and symposia. His research interests include microwave remote sensing for inversion of biophysical parameters, polarimetric and interferometric techniques, and applications of radar remote sensing in agriculture and geophysics.

Dr. Lopez-Sanchez was the recipient of the Indra Award for the best Ph.D. thesis about radar in Spain, in 2001. From 2006 to 2012, he was the Chair of the Spanish Chapter of the IEEE Geoscience and Remote Sensing Society.





**Francesca Ticconi** received the Laurea degree in electronic engineering and the Ph.D. degree in electromagnetism from the University of Rome La Sapienza, Rome, Italy, in 2003 and 2007, respectively.

From July 2003 to October 2005, she was with the Italian Environmental Protection Agency (APAT), analyzing the development of new technologies suitable for minimizing electromagnetic emissions. From November 2007 to September 2008, she was with the Centre of Terrestrial Carbon Dynamics (CTCD), University of Sheffield, Sheffield, U.K., where she

worked on SAR image processing for forest monitoring. After that period, she worked with the German Aerospace Centre, Cologne, Germany, until December 2010, where she studied scattering electromagnetic models for the interpretation of polarimetric and interferometric SAR data. Until May 2013, she was with the School of Earth and Environment, University of Leeds, Leeds, U.K., where she focused on measuring changes of glaciers and Greenland ice sheets by using radar altimetry. From June 2013 until January 2020, she was with the Remote Sensing and Product Division, EUMETSAT, Darmstadt, Germany, where she worked within the scatterometry team on developing the processing algorithms for the product generation of the new EPS-SG scatterometer instrument. Since February 2020, she has been working with ESA in the Wave Interaction and Propagation Section, where she contributes to the performance assessment of several missions (i.e., BIOMASS, CIMR, Rose-L). She is also involved in modeling the effects of the ionosphere on polarimetric Synthetic Aperture Radar (SAR) data and on a correction algorithm for their mitigation. Her research interests include the microwave interaction with natural media and in particular the wave scattering and propagation from the Earth's surface, for the estimation of bio-geophysical parameters. She is also interested in remote sensing of the oceans and the cryosphere.

Dr. Ticconi is a member of the IEEE Geoscience and Remote Sensing Society.



**Nicolas Floury** received the M.Sc. degree in engineering from Télécom ParisTech, Paris, France, in 1993, and the Ph.D. degree in applied physics from the University Paris Diderot, Paris, France, in 1999.

Since then, he has been with the European Space Research and Technology Centre, European Space Agency, Noordwijk, The Netherlands, where he is the Head of the Wave Interaction and Propagation Section. His research interests include signal processing and electromagnetic modeling applied to microwave interaction with natural media.